

國立臺灣大學理學院化學系

碩士論文

Department of Chemistry

College of Science

National Taiwan University

Master Thesis



苯酚的光分解：光解碎片動能分布中慢速產物的來源

Photodissociation of Phenol:

the Origins of Slow Component in Photofragment

Translational Energy Distribution

林彥成

Yen-Cheng Lin

指導教授：李遠哲 博士

倪其焜 博士

Advisor: Yuan-Tseh Lee, Ph.D.

Chi-Kung Ni, Ph.D.

中華民國 106 年 6 月

June, 2017

國立臺灣大學碩士學位論文
口試委員會審定書

(論文中文題目) 苯酚的光分解：光解碎片動能分布中慢速產物的來源

(論文英文題目) Photodissociation of Phenol: the Origins of Slow Component
in Photofragment Translational Energy Distribution

本論文係 林彥成 君 (學號 R04223133) 在國立臺灣大學
化學系完成之碩士學位論文，於民國 106 年 6 月 22 日承下列考
試委員審查通過及口試及格，特此證明。

口試委員：

李遠哲

(簽名)

(指導教授)

王彥蓉

李世煌

曾達銘

倪其煒

陳逸聰

系主任、所長

(簽章)

謝誌



碩班兩年一下就過去了，加上大學時期也在這間實驗室待了 4 年，也到了要畢業離去的時候了。一來走來受到了很多人的幫忙，首先要感謝我的指導教授李遠哲老師與倪其焜老師，謝謝他們放任我去做我想做的事，並且在需要的時候給予適當的建議，與他們的討論時光總是讓我受益良多。其中尤其感謝倪其焜老師對我的不放棄，大學時期做了兩年的實驗最後沒有得到任何成果時，是有一點挫折的，也曾經有想過是否要放棄研究這條路，但是最後還是在老師的建議下留了下來，而後才能有這篇論文的產生，也才能稍稍重燃對研究的熱情。

還要感謝實驗室裡的夥伴，謝謝一起做實驗的李勤，尤其是在同步輻射 24 小時的輪班中，彼此都辛苦了。然後謝謝偶爾會給我一些建議的厚余學長與總是幫忙我力氣活的阿辰學長。也要感謝 509 的點心夥伴們竹平、佳燕、詩珮，謝謝你們給我的各種面向的建議。

另外要感謝在同步輻射的時候幫助我的人們，李世煌老師、李英裕老師、曾建銘老師、黃文建、林竣平還有曾建銘老師的學生們，謝謝你們的協助讓我們在同步輻射的實驗能順利進行，也謝謝你們當我們在同步輻射做實驗時幫我們買便當或是帶我們出去吃飯。

最後要感謝過去許許多多曾經支撐著我心靈的人們，我不是一個堅強的人，常常會遇到挫折想放棄，在那些時候，無論是以怎樣的形式鼓舞我的人們，謝謝你們，因為有你們的存在我才能有辦法走到今天。

中文摘要



因為苯酚是多重位能曲面分解的重要模型分子，其光分解在過去數十年來被許多實驗與理論計算研究過。苯酚在紫外光區域光分解的主要碎片為 OH 斷鍵產生的氫原子與苯氧基。先前的實驗在測量光解碎片動能分布時，發現有兩個不同的產物，他們分別被稱為快速產物與慢速產物。快速產物被認為是苯酚的激發態分解成苯氧基的基態。而慢速產物則有以下兩種可能：(1) 從苯酚的基態分解而來，(2) 從苯酚的激發態分解成苯氧基的激發態。過去並沒有實驗測量這兩種分解途徑的分支比。


在本實驗中，我們藉由改良傳統的光解碎片動能儀完成一新型態的時間解析實驗並得到時間解析的移動動能分布。藉此我們可以很清楚地分出三種不同的分解途徑。分解途徑一在移動動能分布中會在 12000cm^{-1} 有一峰值，並且其生命週期為小於 10 奈秒，因此分解途徑一為苯酚的激發態分解成苯氧基的基態；分解途徑二在移動動能分布中會在 2000cm^{-1} 有一峰值，同樣的其生命週期為小於 10 奈秒，因此分解途徑二為苯酚的激發態分解成苯氧基的激發態；分解途徑三在移動動能分布中主要落於小於 3000cm^{-1} 的區域，而其生命週期為大於 100 奈秒，因此分解途徑三為苯酚的基態分解。根據本實驗的結果，我們可以得到苯酚在基態分解及苯酚在激發態分解成苯氧基的基態、第一激發態、第二激發態的分支比。在 193 奈米分解時分別為 0.05、0.53、0.24 和 0.17；在 213 奈米分解時分別為 0.07、0.60、0.32 和 0。我們得到的這些分支比數值可以做為檢驗理論計算結果的重要依據。而我們所開發出的新方法也有助於研究其他有多重位能曲面分解的分子的光分解。

Abstract



Photodissociation of phenol has been investigated by both experimental and theoretical methods for the past few decades since it is an important model molecular of multistate dissociation. The major photofragments in UV region are Hydrogen atom plus phenoxy radical produced through OH bond fission. Previous experiments showed that there are two components, namely fast and slow, in the photofragment translational energy distributions. The fast component was assigned as dissociation in the electronic excited state forming the ground state phenoxy radical. As for the slow component, it can be assigned as (1) dissociation in the electronic excited state forming the excited state phenoxy radical, or (2) internal conversion followed by dissociation in the electronic ground state. There was no experimental measurement of branching ratio for these two channels before.

In this work, we have performed a new type of time-resolved experiment using modified conventional photofragment translational spectroscopy to get the time-resolved spectra of photofragment translational energy. The results show clear characteristic of three different dissociation channels. The first channel producing a component centered at $\sim 12000 \text{ cm}^{-1}$ in translational energy distribution has a lifetime $< 10 \text{ ns}$, and is assigned as dissociation in the excited state forming the ground state phenoxy radical. The second channel generates a component centered at $\sim 2000 \text{ cm}^{-1}$ in



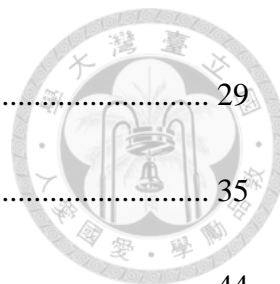
translational energy distribution with a lifetime < 10 ns, and is assigned as dissociation in the excited state forming the excited state phenoxy radical. The third channel producing a component mainly below 3000 cm^{-1} in translational energy distribution has a lifetime > 100 ns, and is assigned as dissociation in the ground state forming the excited state phenoxy radical. Finally, we get the branching ratio of ground state dissociation channel and excited state dissociation channel forming phenoxy radical X,A,B state for the photodissociation of phenol at 193nm as 0.05, 0.53, 0.24, 0.17, and at 213 nm as 0.07, 0.60, 0.32, 0. These branching ratios are useful for justifying the results of theoretical calculations. Furthermore, this technique is useful for the investigation of photodissociation of other molecules which would also dissociate on the multi potential energy surface.

Contents



口試論文審定書	#
謝誌	I
中文摘要	II
Abstract.....	III
Contents	V
List of Figures.....	VII
List of table.....	X
Chapter 1. Introductions	1
Chapter 2. Experimental Method	11
2.1 Experimental Apparatus	11
2.1.1 Conventional Photofragment Translational Spectroscopy (PTS).....	11
2.1.2 Time-of-Flight Mass Spectrometer	13
2.2 Experimental Principle	14
2.2.1 Translational Energy Distribution	14
2.2.2 Time-Resolved Experiment.....	16
2.3 Experimental Procedure and Data Analysis	18
Chapter 3. Photodissociation Experiment of Phenol	26
3.1 Photodissociation Experiment of Phenol at 275 nm.....	26

3.2	Photodissociation Experiment of Phenol at 213 nm.....	29
3.3	Photodissociation Experiment of Phenol at 193 nm.....	35
3.4	Discussions	44
Chapter 4. Prospects.....		49
Chapter 5. Conclusions		52
Reference		53
Appendix A. Changing from Laboratory Frame to Center-of-Mass Frame.....		56



List of Figures



Figure 1-1. Chemical formulas of amino acid tyrosine and phenol.	1
Figure 1-2. 1D Potential energy surface cut of phenol along OH axis.....	2
Figure 1-3. Photodissociation scheme of phenol.....	3
Figure 1-4. Concept of photofragment translational energy distribution	4
Figure 1-5. Translational energy distribution of H elimination channel of phenol at 248 nm photolysis using multi-mass ion imaging apparatus.....	5
Figure 1-6. Translational energy distribution o H elimination channel of phenol at193 nm photolysis using multi-mass ion imaging apparatus.....	6
Figure 1-7. Translational energy distribution of H elimination channel of phenol done by Truhlar <i>et al</i> (simulation) and Ashfold <i>et al</i> (experiment).....	7
Figure 1-8. Translational energy distribution of H elimination channel of phenol done by Ashfold <i>et al.</i> and multi-mass machine.	8
Figure 2-1. Schematic of the conventional photofragment translational spectroscopy. .	12
Figure 2-2. Schematic of the Time-of-flight mass spectrometer.	14
Figure 2-3. Trigger time profile of the experiment.....	19
Figure 2-4. Optimization of the delay time between pump laser and nozzle	19
Figure 2-5. Optimization of the voltage of quadrupole mass filter	20
Figure 2-6. Optimization of the wavelength of dye laser	20



Figure 2-7. Schematic of the time-resolved experiment.....	22
Figure 3-1. H atom TOF spectra at 275 nm.....	26
Figure 3-2. Translational energy distribution of H atom elimination channel at 275nm.	28
Figure 3-3. H atom TOF spectra at 213 nm.....	29
Figure 3-4. Translational energy distribution of H atom elimination channel at 213 nm.	31
Figure 3-5. Intensity change as the function of the pump laser position at 213 nm.....	32
Figure 3-6. Fitting of Relative intensity change of slow component as the function of position at 213 nm.	33
Figure 3-7. Translational energy distribution of excited state dissociation channel at 213 nm.	34
Figure 3-8. Signal change with the angle of laser polarization at 213 nm	35
Figure 3-9. H atom TOF spectra at 193 nm.....	36
Figure 3-10. Translational energy distribution of H atom elimination channel at 193 nm.	38
Figure 3-11. Intensity change as the function of the pump laser position at 193 nm.....	39
Figure 3-12. Time-of-Fight mass spectrum with 193 nm pump and 118 nm probe	40
Figure 3-13. Transient ion yield of (a) $C_5H_5^+$, (b) $C_6H_5O^+$ at 193 nm.....	41




Figure 3-14. Fitting of relative intensity change of slow component as the function of position at 193 nm.	42
Figure 3-15. Translational energy distribution of excited state dissociation channel at 193 nm.	43
Figure 3-16. Signal change with the angle of laser polarization at 193 nm.	44
Figure 3-17. Comparison of ground state dissociation at 193 nm and 213 nm.	45
Figure 3-18. Comparison of excited state dissociation at 193 nm and 213 nm.	47
Figure 4-1. 1D Potential energy surface cut of aniline along NH axis.	50
Figure 4-2. Photofragment translational energy distributions of aniline at 193 nm using (a) H Rydberg atom tagging and (b) multi mass ion imaging.	50
Figure 4-3. Photofragment translational energy distributions of anisole at 193 nm using multi mass ion imaging.	51
Figure A-1. Correlation between laboratory frame and center-of-mass frame.	56

List of table



Table 3-1. Comparison of the branching ratio at 193 nm and 213 nm for different dissociation channel.....	48
---	----



Chapter 1. Introductions

Photodissociation of phenol has been intensely studied at various photolysis wavelengths with both experimental¹⁻¹¹ and theoretical methods¹²⁻²⁰ for a long time due to its importance in many fields. In biochemistry, the photostability against UV irradiation of biomolecules, such as DNA and proteins, are important properties of life. The excited-state relaxation processes of their building blocks, nucleobases and amino acids, are thus highly concerned. Tyrosine and many other aromatic amino acids have strong UV absorption cross-sections but low fluorescence quantum yields²¹⁻²³, meaning that there must be one or more fast nonradiative relaxation processes which would quench the fluorescence effectively. The investigations of excited-state dynamics of amino acids lead to the photochemistry studies of amino acids chromophores such as phenol, the chromophore of tyrosine, as shown in Figure 1-1.

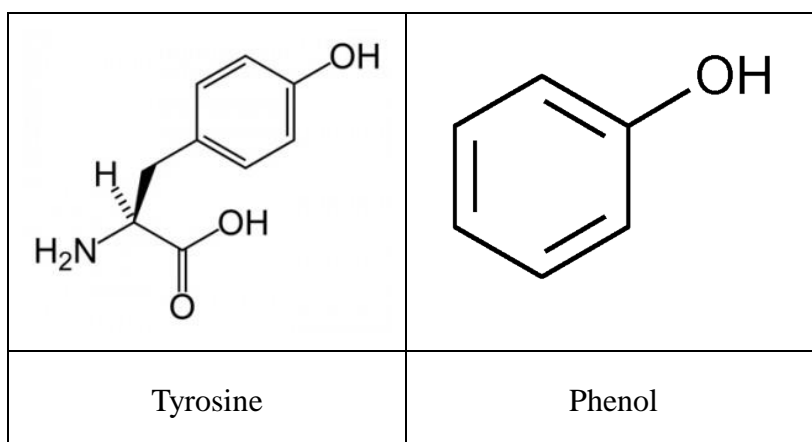
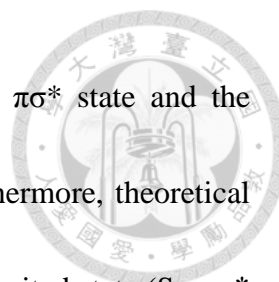


Figure 1-1. Chemical formulas of amino acid tyrosine and phenol.



In quantum chemistry, phenol is the touchstone of repulsive $\pi\sigma^*$ state and the model molecule of excited state hydrogen detachment.^{1-3, 12-13} Furthermore, theoretical calculations of phenol show that the ground state (S_0) and the first excited state (S_1 , $\pi\pi^*$ state) intersect the second excited state (S_2 , $\pi\sigma^*$ state) and generates two conical intersections, as illustrated in Figure 1-2.^{4, 7, 14-20} The resulting potential energy surfaces bring highly interests to physical chemists, and phenol is taken as a model molecule for the theoretical and experimental investigations of molecular dissociation on multistate potential energy surfaces.

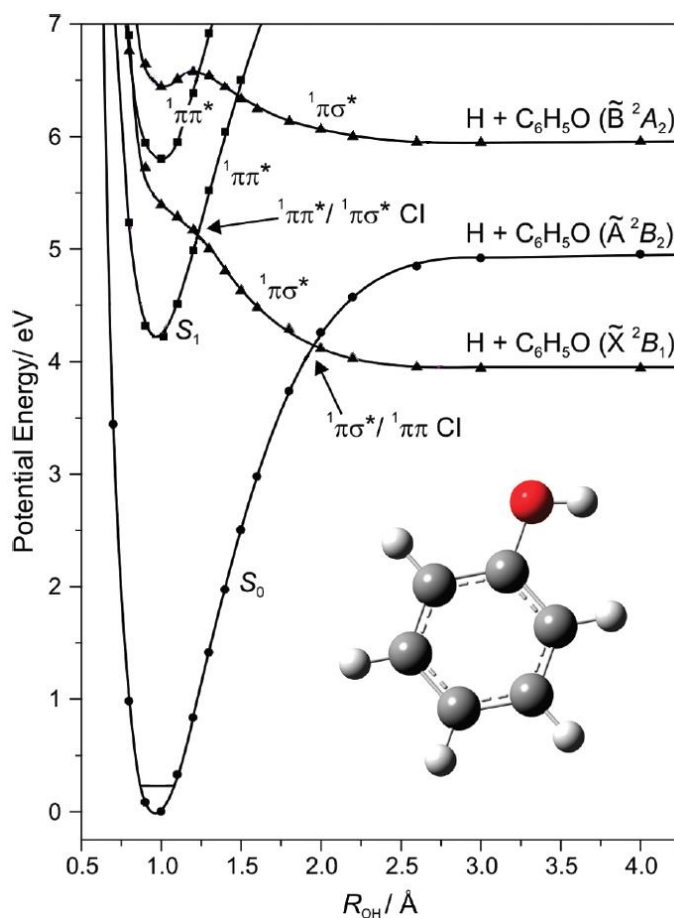
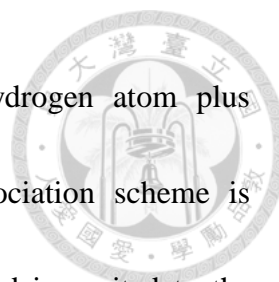


Figure 1-2. 1D Potential energy surface cut of phenol along OH axis.⁷



The main photofragments of phenol in UV region are hydrogen atom plus phenoxy radical through the OH bond fission. A simple dissociation scheme is illustrated in the Figure 1-3. When phenol absorbs one photon and is excited to the electronic excited state (reaction (1-1)), it may dissociate in the excited repulsive state (reaction (1-2)), or undergo internal conversion to the highly vibrational electronic ground state (reaction (1-3)) followed by dissociation in the ground state (reaction (1-4)). Photofragment translational energy distributions are usually used to determine the dissociation pathway. Figure 1-4 shows the concept of it. For dissociation in the repulsive state, the energy would most populate in the translational energy part and thus photofragment translational energy distribution would achieve the maximum available energy of one photon dissociation, which is equal to the photon energy minus bond energy. If molecule undergoes internal conversion, the fast process of intramolecular vibration redistribution would randomize the energy in each degree of the freedom. In such case, the translational energy of fragment would become small.

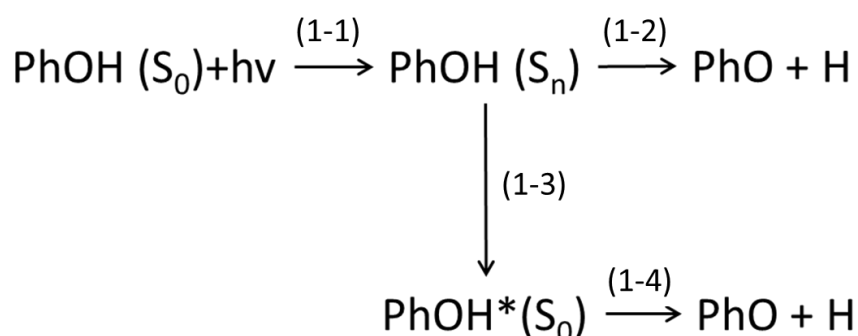


Figure 1-3. Photodissociation scheme of phenol.

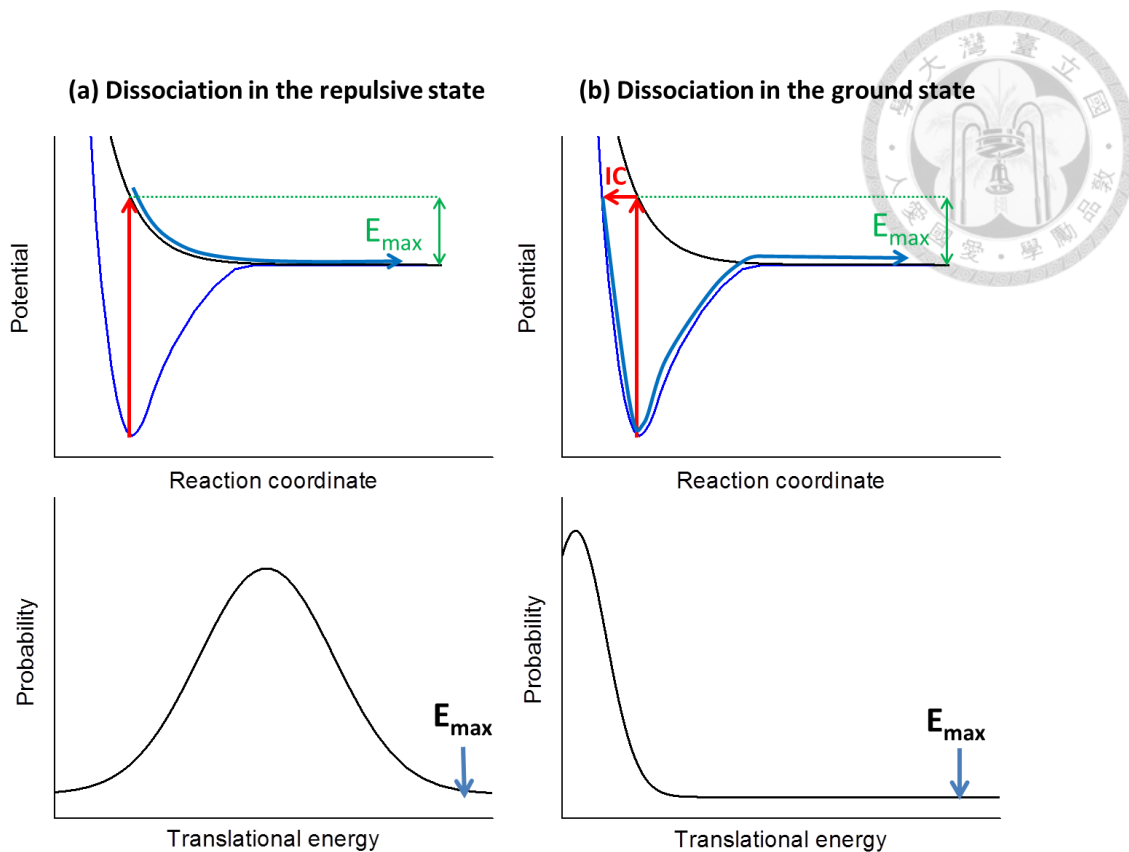


Figure 1-4. Concept of photofragment translational energy distribution

The concept of excited state hydrogen transfer was first proposed by Pino *et al.* in 2000 with the photodissociation experiment of phenol-ammonia cluster.² Later, Sobolewski *et al.* used ab initio calculations to predict the existence of excited repulsive $\pi\sigma^*$ potential and propose a more general mechanism of excited state hydrogen detachment.¹²⁻¹³ In 2004, our group used the homemade multi-mass ion image apparatus to measure the photofragment translational energy distribution of phenol at 248 nm.³ The result shown in Figure 1-5 had a component which achieved the maximum available energy of one photon dissociation. This result provided the first experiment evidence of $\pi\sigma^*$ dissociation channel of phenol (analogous to reaction (1-2)).

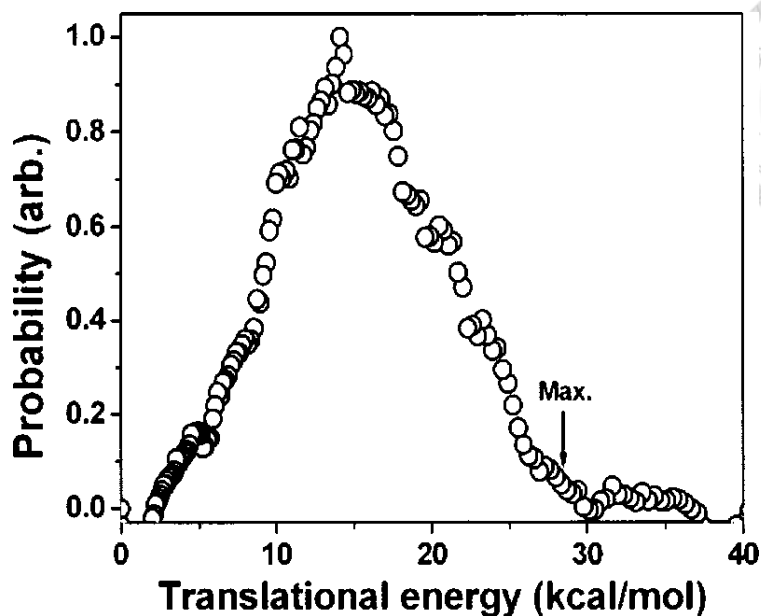


Figure 1-5. Translational energy distribution of H elimination channel of phenol at 248 nm photolysis using multi-mass ion imaging apparatus.³

In 2007, our group further investigated the photodissociation of phenol at 193 nm and found there were three different dissociation channels, ie. H, CO, and H₂O elimination channels.⁵ The latter two were assigned as dissociation in the highly vibrational electronic ground state after internal conversion. The photofragment translational energy distribution of H elimination channel showed a bimodal shape at 193nm as illustrated in Figure 1-6. We name these two components as fast component and slow component here. The fast component which almost achieved the maximum available energy of one photon dissociation was assigned as dissociation in the $\pi\sigma^*$ repulsive state (analogous to reaction (1-2)). The slow component was assigned as dissociation in the highly vibrational electronic ground state after internal conversion (analogous to reaction (1-4)) due to the existence of CO and H₂O elimination channel.

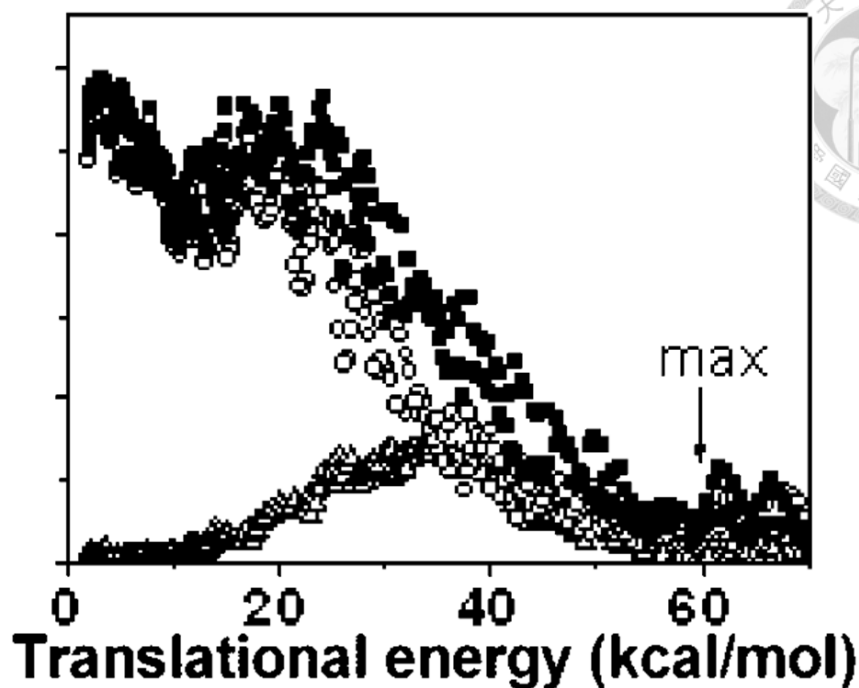


Figure 1-6. Translational energy distribution of H elimination channel of phenol at 193 nm photolysis using multi-mass ion imaging apparatus.⁵

In 2014, Truhlar *et al.* used multistate semiclassical trajectory method to simulate the photodissociation of phenol.¹⁶ They found that if molecule dissociated on the repulsive potential with enough energy, it may have the chance to populate to the first excited state (\tilde{A}^2B_2) of phenoxy radical after passing through the $^1\pi\sigma^*/^1\pi\pi$ conical intersection. This process would also contribute a slow component due to the partition of the energy in the electronic part. They compared their results of translational energy distributions to the experimental data done by Ashfold *et al.* in 2006 as shown in Figure 1-7.⁴ It seemed that the results of theoretical calculation agreed with experimental data very well. They concluded that the slow component was mainly from phenoxy radical produced in the first excited state.

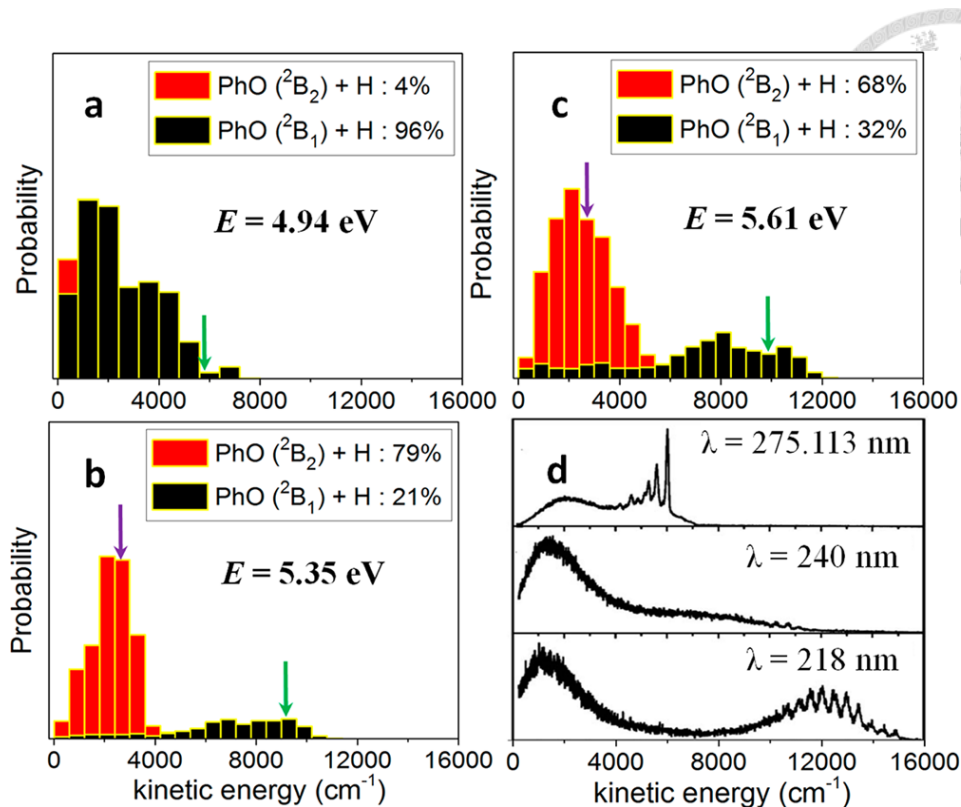
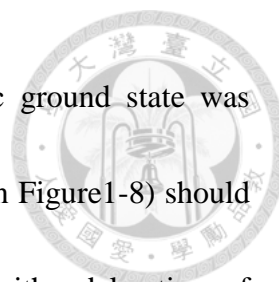


Figure 1-7. Translational energy distribution of H elimination channel of phenol done by Truhlar *et al* (simulation) and Ashfold *et al* (experiment).^{4, 16}

However, there are two problems of this comparison. First, the calculation results only consist of the contribution of dissociation in the repulsive state while experimental data would collect both contributions of dissociation in the repulsive state (analogous to reaction (1-2)) and dissociation in the highly vibrational electronic ground state (analogous to reaction (1-4)) and they will overlap with each other.

Second, we have used the photodissociation of phenol at S_1 band origin as an example to show that the results of Ashfold *et al.* suffer a big problem of background.²⁴

We compare the spectra we take to that of Ashfold *et al.* in the Figure 1-8. The key point is that our pump-probe delay time is 100 μ s while Ashfold *et al.* used a pump-probe



delay time of 10 ns. The lifetime of highly vibrational electronic ground state was measured as 62 μs .²⁴ That is the slow component (the green curve in Figure 1-8) should not generate within a delay time of 10 ns and the distribution taken with a delay time of 10 ns should look like the blue curve in Figure 1-8. Thus, the slow component of Ashfold *et al.* is mainly due to an unintended multi-photon background. The background is generated when probe laser shines on the undissociated metastable phenol:

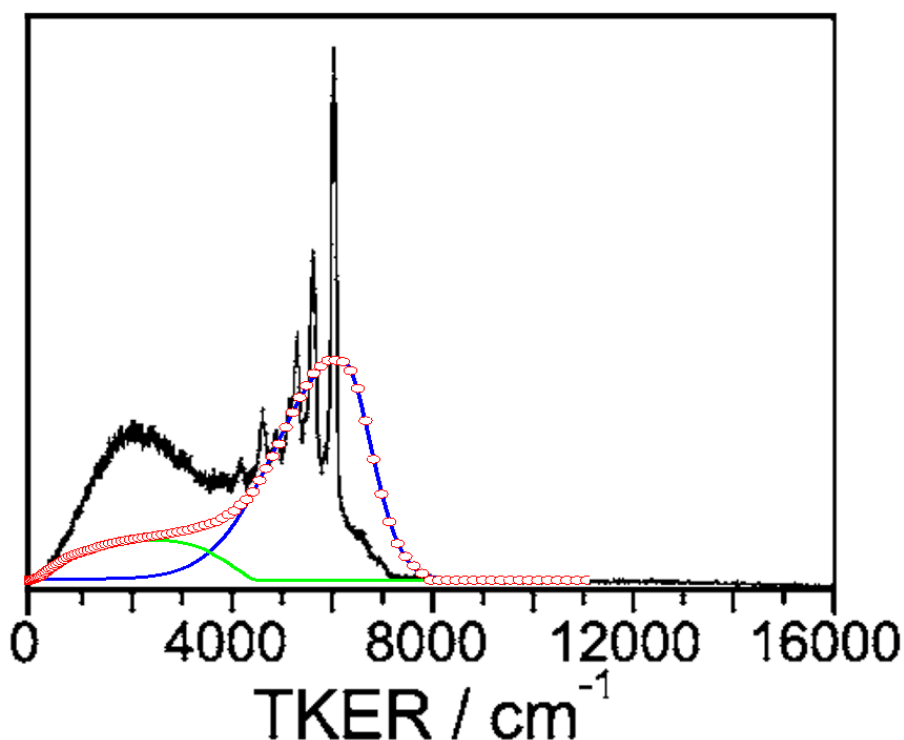
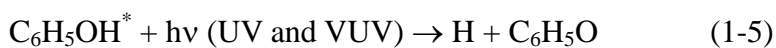




Figure 1-8. Translational energy distribution of H elimination channel of phenol done by Ashfold *et al.* (black line) and multi-mass machine (red dot). The blue line and green line are the deconvolution result of red dot.²⁴



The motivation of this work is to find the contribution to the slow component of dissociation in the excited state (analogous to reaction (1-2)) and dissociation in the ground state (analogous to reaction (1-4)) respectively to give a clearer picture of photodissociation dynamics of phenol.

An intuitive thought for measuring the separate contributions from reactions (1-2) and (1-4) is the typical time-resolved pump-probe experiments. Reaction (1-2) occurs on a repulsive excited potential and thus the dissociation lifetime is short, typically less than few nanoseconds.^{7, 25} In contrast, dissociation rate of reaction (1-4) is slow. For a molecule like phenol which has many vibrational degrees of freedom, the dissociation lifetimes can range from submicroseconds to several hundred microseconds depending on the photon energy.^{5, 24} When the pump-probe delay time is shorter than the lifetime of reaction (1-4), the detected products are mainly generated from reaction (1-2). As the delay time increases, the detected products come from both reactions (1-2) and (1-4). By comparing the measurements from different pump-probe delay times, it is possible to obtain the separate contributions of reactions (1-2) and (1-4). However, the pump-probe delay time shorter than the lifetime of reaction (1-4) may cause the potential background (analogous to reaction (1-5)) and such method cannot obtain accurate branching ratio.



In this work, we demonstrate a new type of time-resolved experiment. We modify the conventional photofragment translational spectroscopy (PTS) by changing the interaction region of pump laser beam and molecular beam. We can select the product generated from a specific time window after excitation. Because the molecule beam does not pass through the probe beam region, it is free from the interference of background produced by undissociated metastable molecules (analogous to reaction (1-5)). We use this technique to measure the translational energy distributions and branching ratios of phenoxy radical produced in the X, A, and B states for the photodissociation of phenol at 213 and 193 nm.

Chapter 2. Experimental Method

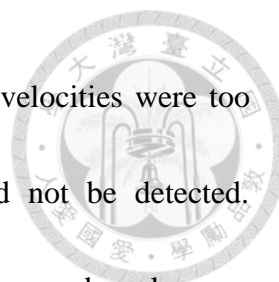
2.1 Experimental Apparatus



2.1.1 Conventional Photofragment Translational Spectroscopy (PTS)

The PTS setup is located at BL21A1, National Synchrotron Radiation Research Center (The Taiwan Light Source) in Hsinchu, Taiwan, and has been described elsewhere previously.²⁶⁻²⁸ Here, only a brief description is given. This apparatus consisted of two source chambers, a differential pumped chamber, main chamber, and detection chamber. In this study, we only used one source chamber to generate the molecular beam and its axis was set perpendicular to the detection axis. The other source chamber was not used. The nozzle, skimmer, and cold finger behind the skimmer of the second source chamber were removed to avoid any reflection of H atom from these devices to detector. The schematic of this apparatus is showed in Figure 2-1.

Phenol was heated to 358 - 363 K, and its vapor was carried by helium at a pressure of 14 - 15 psi. The phenol/He mixture was then expanded by an Even-Lavie valve and then entered main chamber. Phenol molecules in the molecular beam were then pumped by 275.11 (S_1 band origin), 213, or 193 nm laser beam. Fragments that flew into the detection chamber were ionized by synchrotron VUV photons at energy 15 eV. Since the detection axis was set perpendicular to the molecular beam, only the lightest fragments, H atom, could fly into the detection chamber and be ionized. For



other heavier fragments, for example, phenoxy radical, the recoil velocities were too low for them to fly into the detection chamber and they could not be detected.

Following the ionization of H atoms, H^+ ions were selected using a quadrupole mass filter and detected by a Daly-type ion counter. In this setup, the undissociated excited phenol ($C_6H_5OH(S_0^*)$) did not pass through the ionization region. Therefore, no background associated with the hot parent molecules (analogous to reaction (1-5)) was produced.

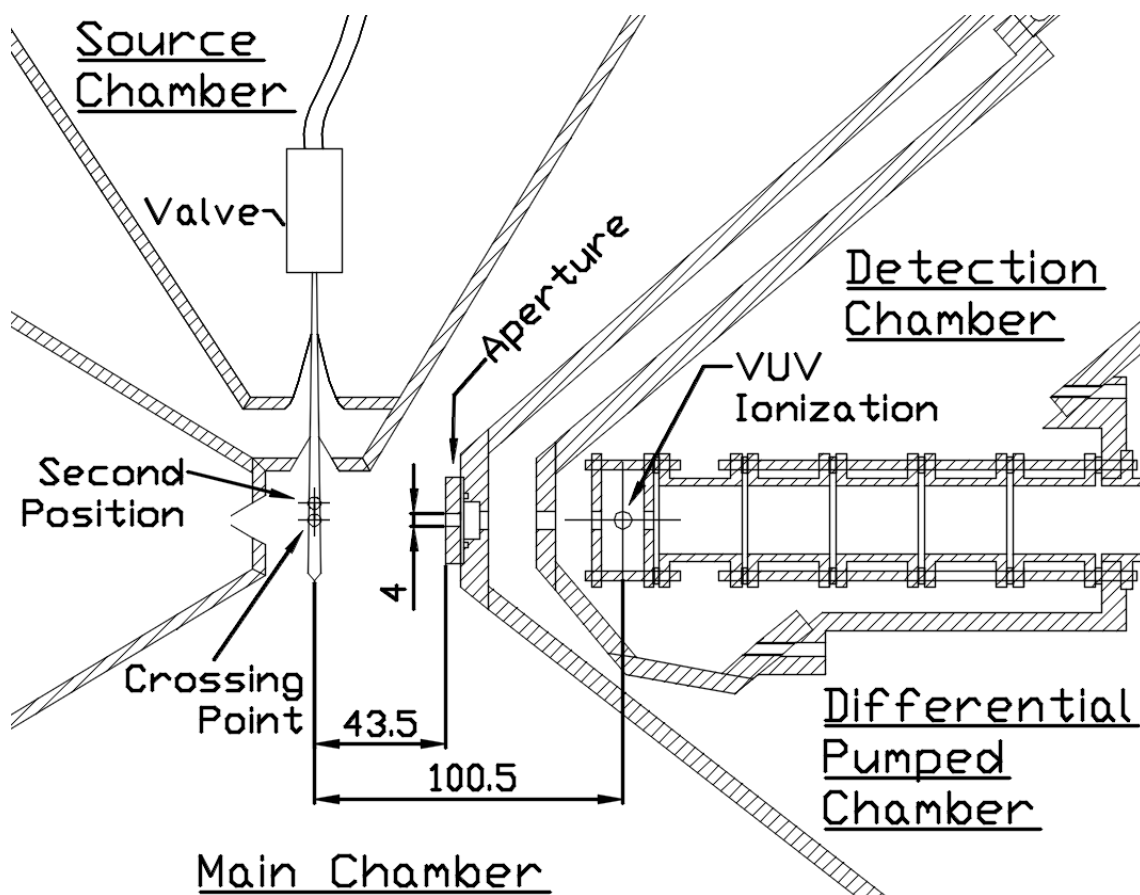
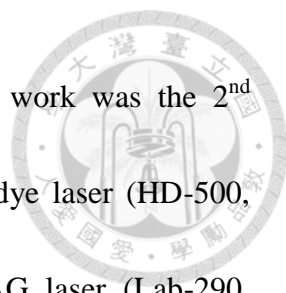


Figure 2-1. Schematic of the conventional photofragment translational spectroscopy.



The UV laser beam of wavelength 275.11 nm used in this work was the 2nd harmonic of a 550.22 nm laser beam, which was produced by a dye laser (HD-500, Lumonics Inc., Canada) pumped by the 3rd harmonic of Nd:YAG laser (Lab-290, Spectra Physics, USA). For the laser beam of wavelength 213 nm, it was obtained by sum-frequency mixing of the 2nd and 3rd harmonics from a Nd:YAG laser (Lab-290, Spectra Physics, CA, USA) in a 5th harmonic generator (LG105, Del Mar Photonics, CA, USA). The 193 nm laser beam was generated by excimer laser (LPF 220, Lambda Physik, Low Saxony, Germany). The polarization of pump laser was changed by a waveplate for 213 nm and polarizer for 193 nm to measure the anisotropic parameter β_2 .

2.1.2 Time-of-Flight Mass Spectrometer

The lifetime of hot phenol, C₆H₅OH (S_0^*), was measured using a separate apparatus: a time-of-flight mass spectrometer and a pulsed VUV laser beam apparatus as illustrated in Figure 2-2. The pump laser beam of wavelength 193 nm was generated by another excimer laser (Compex Pro 205, Coherent, CA, USA). The 355 nm laser beam from the third harmonic of a Nd:YAG laser (Lab-190, Spectra Physics, CA, USA) was focused into a Xe cell to generate the probe laser photons at 118.2 nm. Phenol vapor was mixed with 450 mTorr of neon at room temperature then pulsed by a general valve.

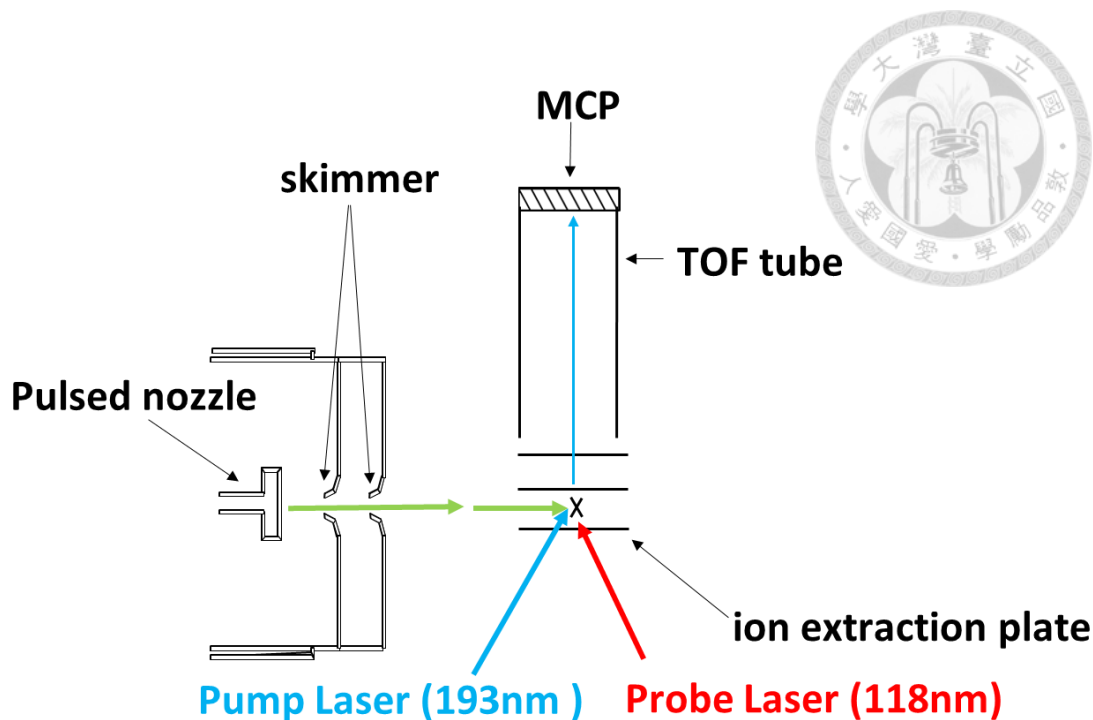


Figure 2-2. Schematic of the Time-of-flight mass spectrometer.

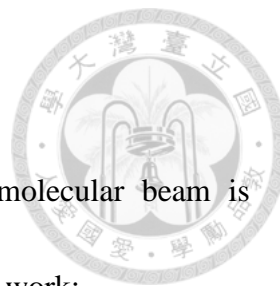
2.2 Experimental Principle

2.2.1 Translational Energy Distribution

The PTS setup can get the photofragment translational energy distribution by recording the arrival time of fragments. Because flight distance is a constant in this setup, Time-of-Flight (TOF) can be converted to the velocity in the laboratory frame:

$$v_{\text{Lab}} = \frac{d}{t} \quad (2-1)$$

where d is the distance from crossing point to the ionization region and is 100.5 mm in this setup, and t is the flight time of the fragment. Because the detection axis is set perpendicular to the molecular beam axis, the velocity in the laboratory frame can be converted to the recoil velocity in the center-of-mass frame:



$$v_{C.M} = \sqrt{v_M^2 + v_{Lab}^2} \quad (2-2)$$

where v_M is the velocity of molecular beam. The velocity of molecular beam is calculated with the following formula²⁹ and is about 1500 m/s in this work:

$$v_M = \sqrt{\frac{2R}{W} \frac{\gamma}{\gamma-1} T_0} \quad (2-3)$$

where R is the gas constant, W is the molecular weight, γ is Heat capacity ratio, and T_0 is the temperature of nozzle. The recoil velocity in the center-of-mass frame is then converted to the translational energy of fragment:

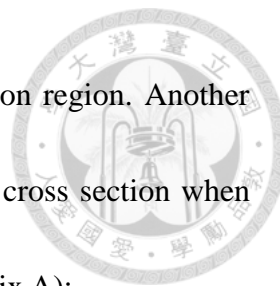
$$E_1 = \frac{1}{2} m_1 v_{C.M.}^2 \quad (2-4)$$

where m_1 is the mass of the measured fragment. The total translational energy released for certain dissociation channel is the sum of the translational energy of two counter fragments and according to the conservation of the momentum it can be written as:

$$E_{trans} = E_1 + E_2 = \frac{1}{2} m_1 \left(1 + \frac{m_1}{m_2}\right) v_{C.M.}^2 \quad (2-5)$$

where m_1 and m_2 are the mass of counter fragment 1 and 2.

Use equation (2-1)~(2-5), we can convert the TOF spectra to the translational energy distribution. A jacobian factor of t^3 is needed to transform the time domain to an energy domain, and a sensitivity correction factor t^{-1} of this setup has to be considered. The sensitivity correction factor is presented because the ionization source can be regarded as continuum light source and the photon number irradiating on the molecule



is proportional to the time the molecule flying through the ionization region. Another correction which should be considered is the change of differential cross section when project the laboratory frame to the center-of mass frame (see Appendix A):

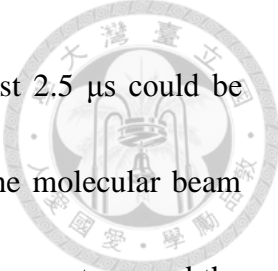
$$\frac{d\sigma}{d\Omega_L} = \frac{d\sigma}{d\Omega_{C.M.}} \sqrt{1 - \left(\frac{v_M}{v_{C.M.}}\right)^2} \quad (2-6)$$

where σ is the reaction cross section, Ω_L is the solid angel in the laboratory frame, and $\Omega_{C.M.}$ is the solid angel in the center-of mass frame. The final factor needed to change the raw TOF spectra to the translational energy distribution is thus:

$$f(t)dt = \frac{t^2}{\sqrt{1 - \left(\frac{v_M}{v_{C.M.}}\right)^2}} f(E)dE \quad (2-7)$$

2.2.2 Time-Resolved Experiment

As for the time-resolved ability of this machine, it is achieved by the restriction of physical dimensions. The VUV probe beam was approximately 1 mm in diameter and located 100.5 mm from the crossing point of molecular beam and pump laser beam. There was an aperture of 4X4 mm between the detection chamber and reaction chamber. The acceptance angle of the aperture enabled to select the H atoms generated in specific time window after the excitation by pump laser because the undissociated metastable molecule would fly with the molecular beam. When the pump laser was at the crossing



point, as illustrated in Figure 2-1, the H atoms generated at the first 2.5 μs could be detected. The time window of product for detection depended on the molecular beam velocity, beam size of pump laser at the crossing point, the size of the aperture, and the VUV beam size. Molecular beam flew away from the acceptance angle of the detector after 2.5 μs ; thus, any fragments subsequently produced from these phenol molecules could not be detected. When the pump laser was moved 5.5 mm upstream along the molecular beam, as illustrated by the second position in Figure 2-1, H atoms generated after the excitation from 0.5 μs to 6.5 μs can be detected. In such arrangement, we were able to detect the H atom produced in different time window by changing the position of pump laser beam to various positions along the molecular beam. The dissociation channels of different lifetimes, i.e. >100 ns and <10 ns, can thus be differentiated.

Anisotropic parameter β_2 is also calculated to have additional information about the lifetime scale by measuring the signal change with the angle of laser polarization and fit with the equation (8):³⁰

$$I(\theta) = 1 + \beta_2 \left(\frac{3}{2} \cos^2 \theta - \frac{1}{2} \right) \quad (2-8)$$

The non-zero anisotropic parameter β_2 exists when the dissociation lifetime is comparable to the rotational time period, which is usually less than 100 ps.

2.3 Experimental procedure and data analysis



In the experiment, we first optimized the conditions to get the best signal-to-noise ratio. Delay time between photolysis laser and nozzle needed to be optimized. The trigger time profile for the experiment is shown in Figure 2-3. We changed the delay time by changing the trigger time of nozzle. The intensity of signal changed as we changed the delay time as shown in Figure 2-4. The delay time would be different with different nozzle temperature, nozzle voltage, nozzle duration, back pressure, and the vapor pressure of the sample. The voltage of quadrupole mass filter was also optimized. Within the adjustment of the voltage of quadrupole mass filter, both intensity of signal and noise would change. Thus, we plot the signal-to-noise ratio rather than signal as the function of voltage as shown in Figure 2-5. The voltage of quadrupole mass filter was only related to the mass of the fragment. For the photodissociation experiment at 275 nm we used the dye laser to produce the laser beam to pump phenol to its S_1 band origin and the actual wavelength used need to be scanned and optimized as shown in the Figure 2-6.

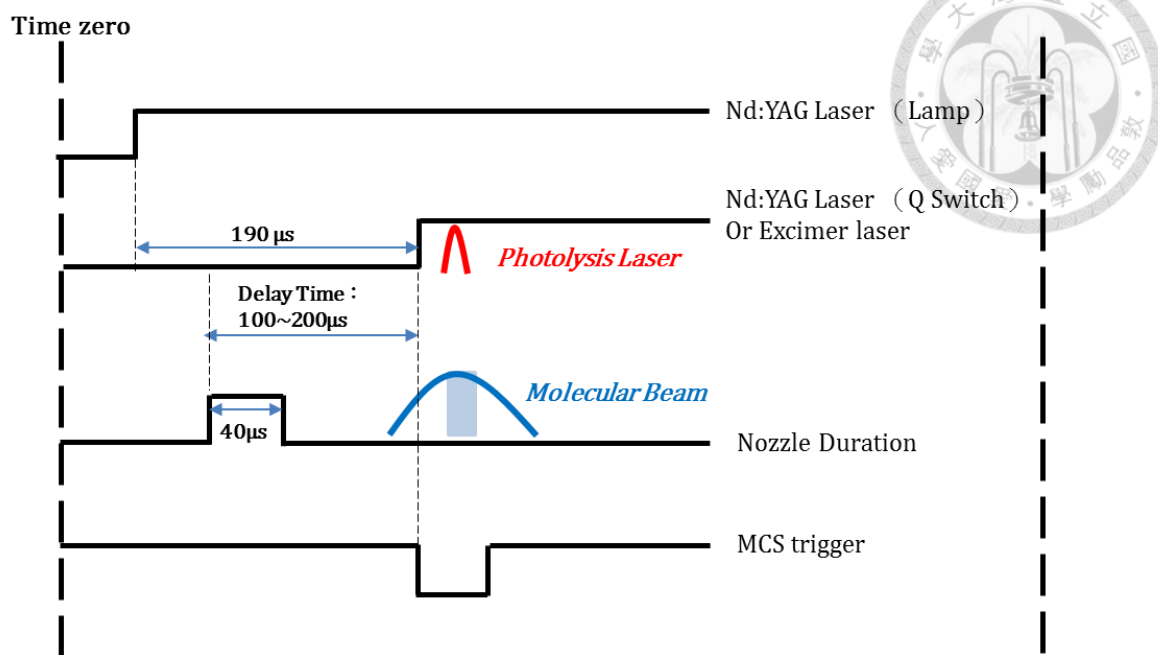


Figure 2-3. Trigger time profile of the experiment.

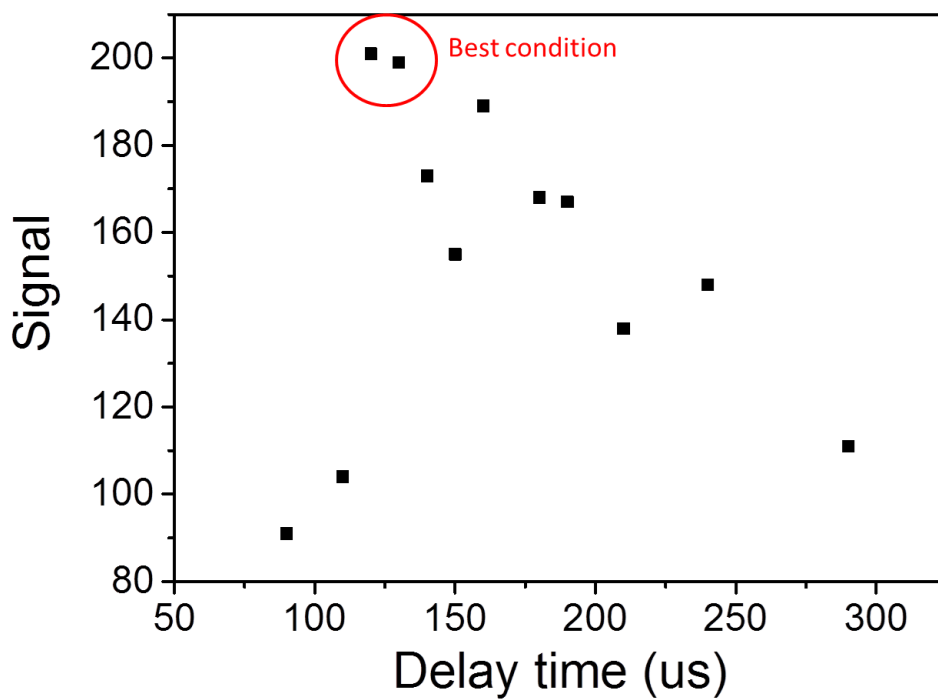


Figure 2-4. Optimization of the delay time between pump laser and nozzle

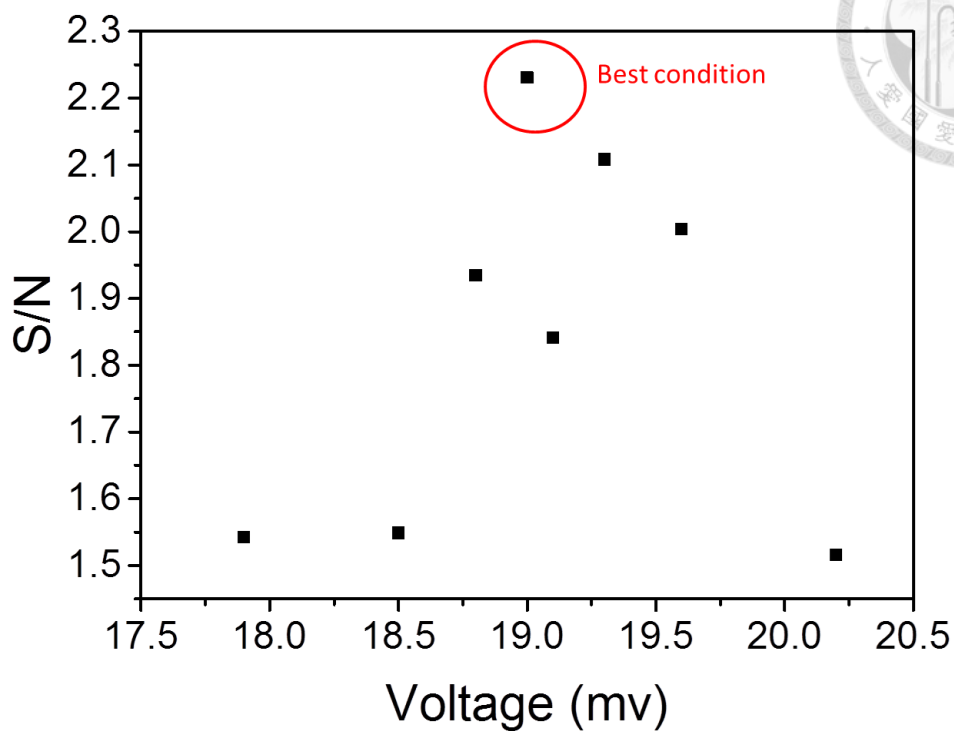


Figure 2-5. Optimization of the voltage of quadrupole mass filter

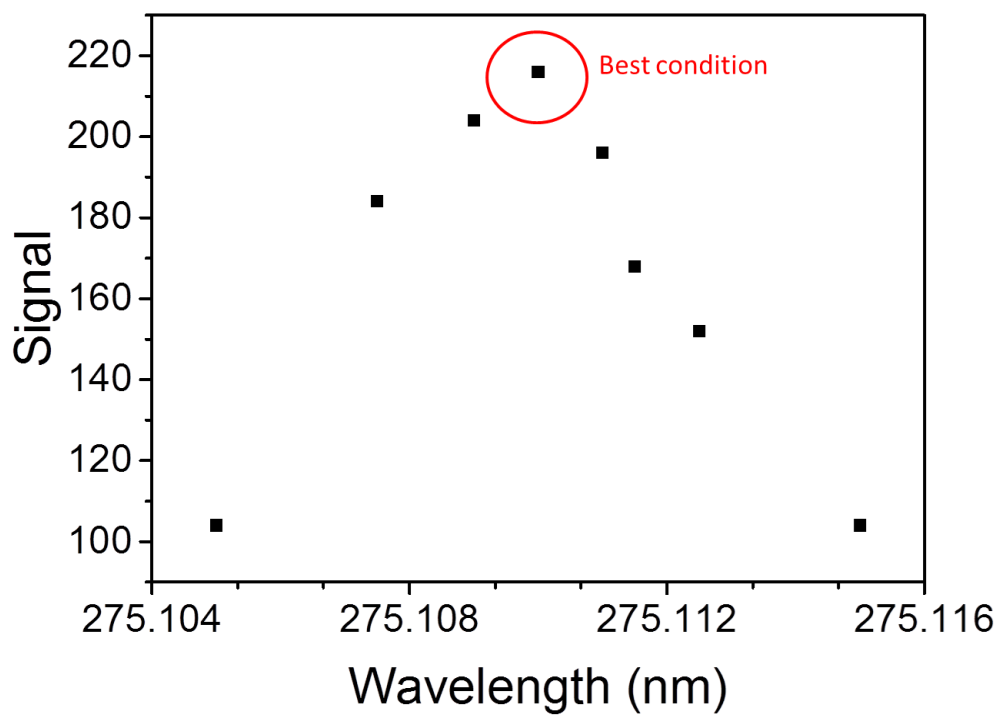



Figure 2-6. Optimization of the wavelength of dye laser



After we optimized the conditions, we measured the TOF spectra at different laser position and calculated the translational energy distribution for two different positions, at crossing point and at a position upstream of molecular beam outside the acceptance angle. For the trigger time profile used in the Figure 2-3, the time recorded by the MCS was not equal to the ion flight time from crossing point to the ionization region. The delay time between trigger and laser shot (about 0.3 μs for YAG laser and 1.2 μs for excimer laser) and the ion flight time within the quadrupole (about 5.4 μs for H^+) should be subtracted to get the true TOF spectra. For the spectrum taken at the crossing point, it mainly detected the fragment generated at the first 2.5 μs and both dissociation channel with long lifetime (>100ns) and short lifetime (<10 ns) would contribute. As for the spectrum taken at a position upstream of molecular beam outside the acceptance angle, for example 5.5 mm upstream of the molecular beam, it mainly detected the fragment generated at 0.5 μs to 6.5 μs and only the dissociation channel with long lifetime (>100ns) would contribute. We can use the spectrum taken at second position with proper factor to make a subtraction of dissociation channel with long lifetime from spectrum taken at the crossing point to get the pure spectrum of dissociation channel with short lifetime. To achieve this, we measured the signal change at several pump laser position and used this data to find the branching ratio and lifetime for the dissociation channel with long lifetime. It is described as following.

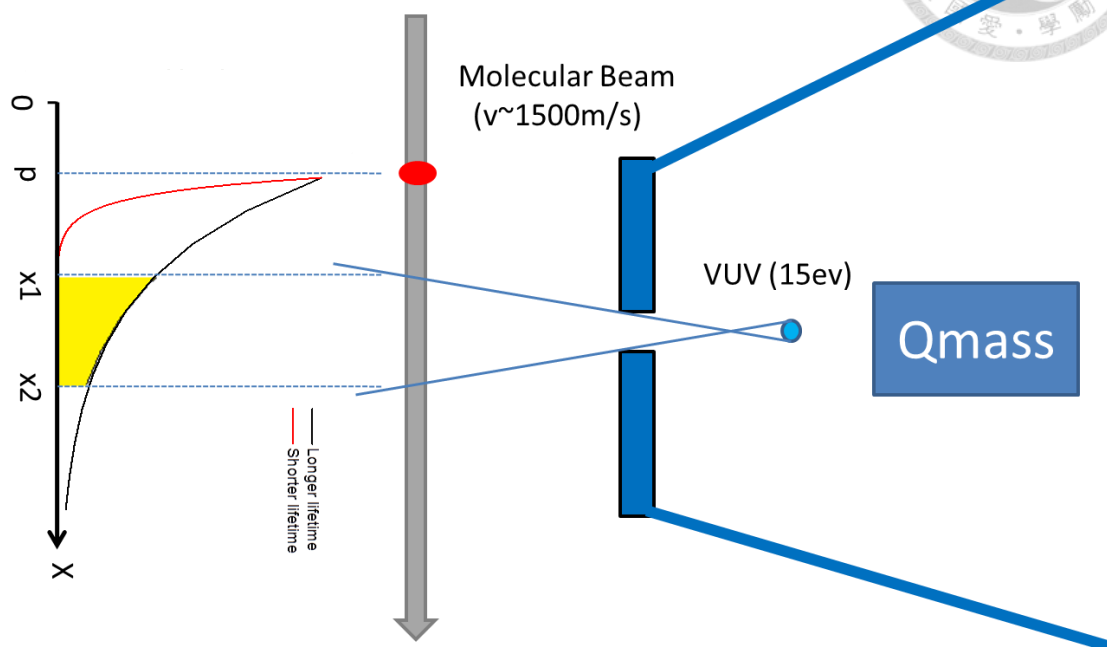


Figure 2-7. Schematic of the time-resolved experiment

Molecular beam can be assumed to be homogeneous in the region irradiated by pump laser beam because the length of the molecular beam (6-10 cm) is much larger than the diameter of pump laser beam (1 mm). According to the relative positions of molecular beam, the interaction region between pump laser beam and molecular beam, and the detector acceptance region, as illustrated in Figure 2-7, only the molecules which dissociate within the detector acceptance region can make contribution to the signal. The signal obtained from an infinite small part of pump laser beam at position r for a given dissociation channel with a rate constant k is proportional to the number of molecules which dissociate within the detector acceptance region:



$$s(p,r) \propto I(p-r) \times k' \int_{x_1 \text{ or } r}^{x_2} e^{-k'(x-r)} dx \quad (2-9)$$

where p is the center position of pump laser beam, $I(x)$ is the pump laser intensity distribution along the molecular beam, $k'=k/v$, k is the unimolecular reaction rate constant, and v is the velocity of molecular beam. The integration region of x is from x_1 (if $r < x_1$) or r (if $r > x_1$) to x_2 . The total signal for a pump laser beam centered at position p is the integration of whole pump laser beam :

$$S(p) = c_0 \int_{-\infty}^{x_2} I(p-r) \times k' \int_{x_1 \text{ or } r}^{x_2} e^{-k'(x-r)} dx \quad dr = c_0 \int_{-\infty}^{x_2} \int_{x_1 \text{ or } r}^{x_2} I(p-r) \times k' e^{-k'(x-r)} dx dr \quad (2-10)$$

where c_0 is a constant. Substitution of $x' = (x-r)$ into Equation (2-10) gives the Equation (2-11)

$$S(p) = c_0 \int_{-\infty}^{x_2} \int_{(x_1-r) \text{ or } 0}^{x_2-r} I(p-r) \times k' e^{-k'x'} dx' dr = c_0 \int_0^{\infty} \int_{x_1-x'}^{x_2-x'} I(p-r) \times k' e^{-k'x'} dr dx' \quad (2-11)$$

When k' is very large (i.e., the short dissociation lifetime), only the integration satisfying the conditions of $x'=0$ makes contribution. Equation (2-11) can be simplified to Equation (2-12):

$$S(p) \approx c_0 \int_0^{\infty} \int_{x_1-x'}^{x_2-x'} I(p-r) \times \delta(x') dr dx' = c_0 \int_{x_1}^{x_2} I(p-r) dr \quad (2-12)$$

Equation (2-12) shows that the signal is only related to the distribution of pump laser beam, the detector acceptance region x_1 and x_2 . It is not related to the molecular property, e.g., dissociation lifetime. We define the instrument response function as $D(p)$.



$$D(p) \equiv \int_{x_1}^{x_2} I(p-r)dr \quad (2-13)$$

If k' is small, the part of the pump laser beam which distributed outside the detector acceptance region, i.e., $r < x_1$ or $x' > 0$, also can make contribution. This is because the dissociation rate is slow such that molecules excited by pump laser beam at the position outside the detector acceptance region can fly into the acceptance region and dissociation occurs at the region between x_1 and x_2 . Substituting $r' = r+x'$ and Equation (2-13) into Equation (2-11) gives the Equation (2-14):

$$\begin{aligned} S(p) &= c_0 \int_0^\infty \int_{x_1}^{x_2} I(p - (r' - x')) \times k' e^{-k'x'} dr' dx' = c_0 \int_0^\infty \int_{x_1}^{x_2} I((p + x') - r') \times k' e^{-k'x'} dr' dx' \\ &= c_0 \int_0^\infty D(p + x') \times k' e^{-k'x'} dx' \end{aligned} \quad (2-14)$$

In the experiment, three components would contribute to the translational energy distribution. Two of them have large k' values and the other has small k' value, the total signal from these three components in translational energy distribution is

$$\begin{aligned} S_t(p) &= S_1(p) + S_2(p) + S_3(p) \\ &= C_1 \times D(p) + C_2 \times D(p) + C_3 \times \int_0^\infty D(p + x') \times k' e^{-k'x'} dx' \end{aligned} \quad (2-15)$$

where component 1,2,3 are dissociation in the excited state forming ground state, excited state phenoxy radical, and dissociation in the ground state respectively. C_i is the relative branching ratio of each component when the pump laser beam size is much smaller than the detector acceptance region, $x_2 - x_1$.



The fast component in the translational energy distribution is contributed from first term on the right side of in Equation (2-15). The measurement of the fast component as a function of pump laser position directly provides the information of $D(p)$. All the instrument related parameters, x_1 , x_2 , all $I(p)$ are in $D(p)$. The last two terms on the right side of in Equation (2-15) make the contribution to the slow component. When $p < x_3$ (depending on the experimental result), $D(p) = 0$. Most of the signal results from the third term of the right side of Equation (2-15). We fit the intensity of slow component as the function of pump laser position when $p < x_3$ with the third term of Equation (2-15) to get the relative branching ratio C_3 and k' (related to the unimolecular dissociation rate constant) of ground state dissociation channel. After that, we calculate the contribution of ground state dissociation channel at crossing point using C_3 , k' , and $D(p)$:

$$S_3(0) = C_3 \times \int_0^{\infty} D(x') \times k' e^{-k'x'} dx' \quad (2-16)$$

Subtraction of ground state contribution at crossing point from translational energy distribution gives the contribution of component 1 and 2. Finally we deconvolution the component 1 and 2 in the translational energy distribution using Gaussian function to get their relatively branching ratio C_1 and C_2 .

Chapter 3. Photodissociation Experiment of Phenol

3.1 Photodissociation Experiment of Phenol at 275 nm

The H atom TOF spectra are illustrated in Figure 3-1 for two pump laser positions, at the crossing point (0 mm) and at the second position (8 mm upstream of molecular beam). Two components in the TOF spectrum of 0 mm can be observed: a sharp and fast component (component I) at arrival time 8-12 us and a broad and slow component (component II) located from 10 us to 25 us. The TOF spectrum of 8mm looks the same as that of 0mm.

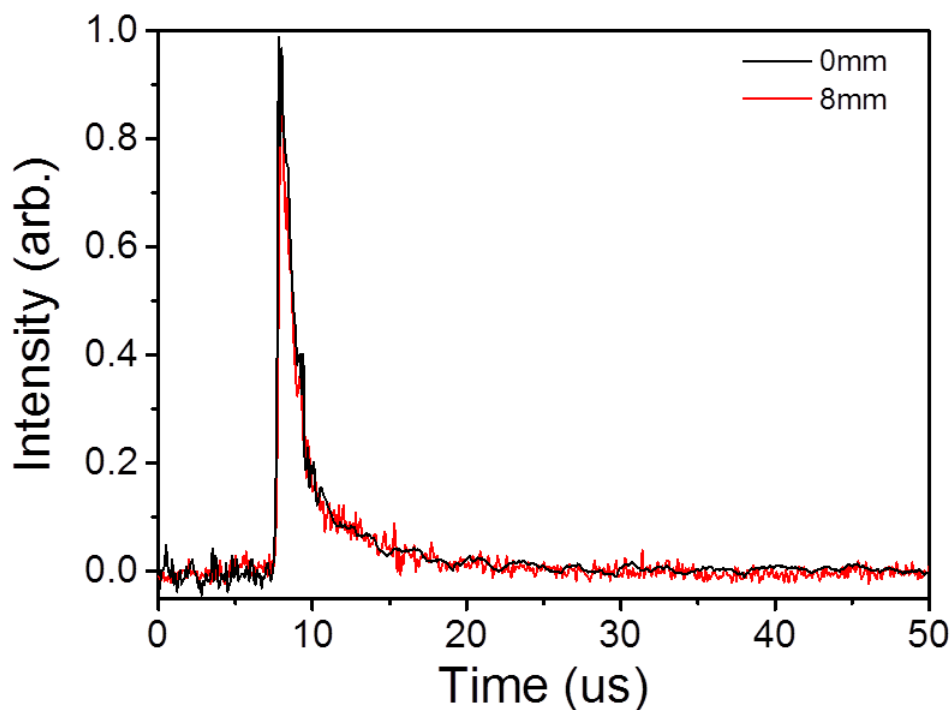
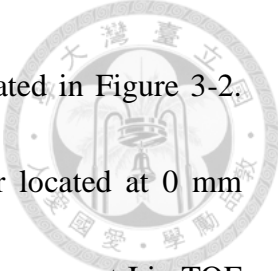


Figure 3-1. H atom TOF spectra at 275 nm. Black line represents the spectrum at crossing point. Red line represents the spectrum at 8 mm upstream of molecular beam. The intensity of different positions are scaled with different factor for comparison



The corresponding translational energy distributions are illustrated in Figure 3-2.

The translational energy distribution obtained from the pump laser located at 0 mm shows two components. The fast component, corresponding to the component I in TOF spectra, centers at $\sim 6000\text{ cm}^{-1}$ and reaches the maximum available energy. We assigned the fast component as dissociation in the electronic excited state forming electronic ground state phenoxy radical product. The slow component with translational energy $< 4000\text{ cm}^{-1}$, corresponds to the component II in TOF spectra. Because the photon energy of 275.11 nm does not have enough excess energy to populate the excited state of phenoxy radical, it can be assigned as dissociation in the ground state or the tail of component I. The translational energy obtained from the pump laser beam located at 8 mm is similar to that of 0mm. Because the acceptance angle of the detector, the fragments forming in the first $2.5\ \mu\text{s}$ were detected when pump laser was located at 0 mm, while the fragments forming in the $1.5\text{-}6.5\ \mu\text{s}$ were detected at 8 mm. The relative ratio of dissociation in the ground state to the dissociation in the excited state should increase as we move the pump beam up. Yet, the spectra taken at 0mm and 8mm look the same. This may indicate the component II just the tail of component I and we don't observe the signal related to the ground state dissociation. It may be due to the small detection time window of about $5\ \mu\text{s}$. The lifetime of highly vibrational electronic ground state was determined as $62\ \mu\text{s}$ ²⁴ and thus only about 8 % of the molecules

dissociation within $5\mu\text{s}$. For this experiment, we conclude that this method is not a good method for probing dissociation channel with lifetime large than $10\mu\text{s}$.

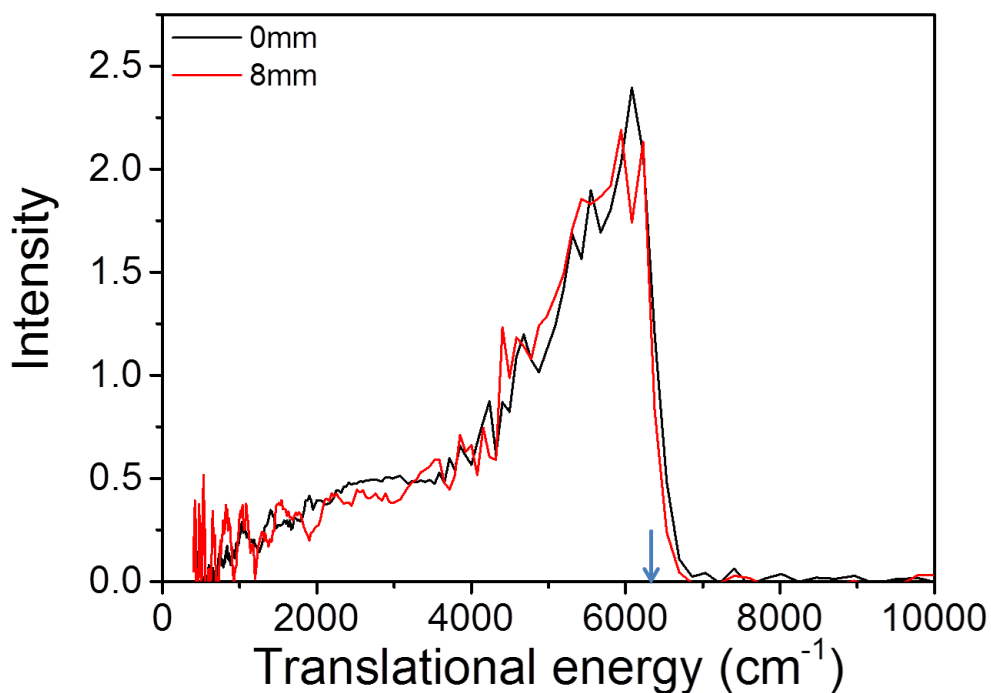
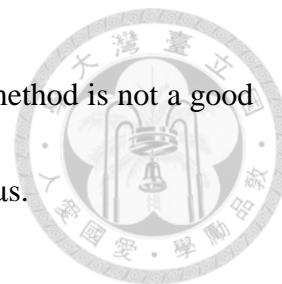


Figure 3-2. Translational energy distribution of H atom elimination channel at 275nm. Vertical arrows indicate the maximum available energy of one photon dissociation to the phenoxy radical ground state. Black line represents the spectrum at crossing point. Red line represents the spectrum at 8mm upstream of molecular beam. The intensity of different positions are scaled with different factor for comparison

3.2 Photodissociation Experiment of Phenol at 213 nm



The H atom TOF spectra are illustrated in Figure 3-3 for two pump laser positions, at the crossing point (0 mm) and at the second position (5.5 mm upstream of molecular beam). Two components in the TOF spectrum of 0 mm can be observed: a sharp and fast component (component I) at arrival time 5-10 μs and a broad and slow component (component II) located from 10 μs to 30 μs . When the pump laser was moved 5.5 mm upstream of the molecular beam, the shape of the TOF spectra changed. The components I and II in the TOF spectrum become small and the third component (component III) located in the region from 20 μs to 100 μs can be clearly observed.

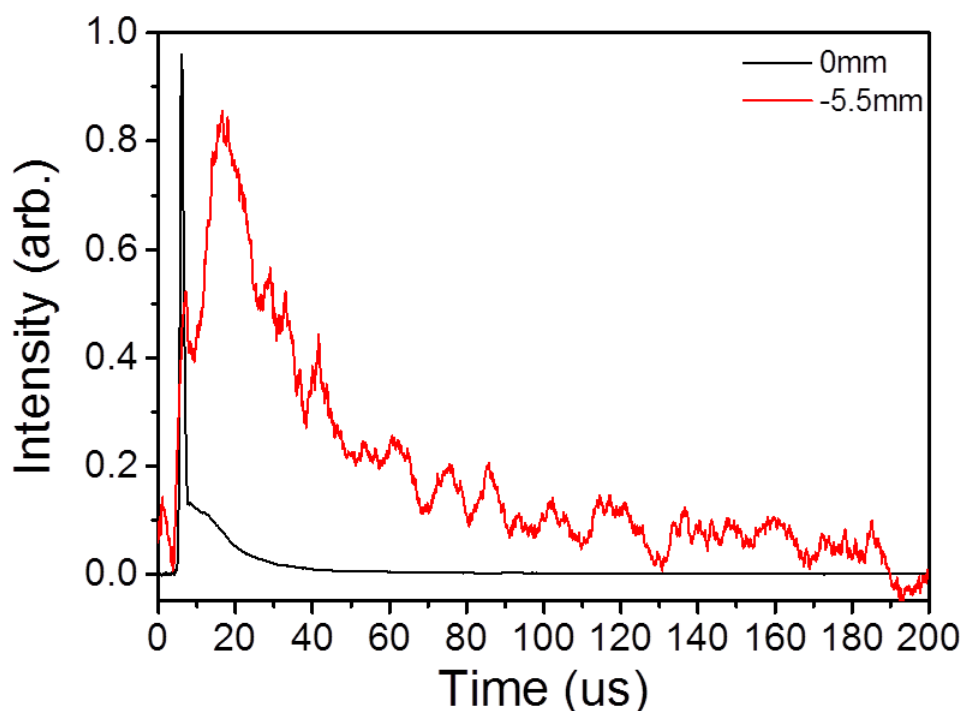

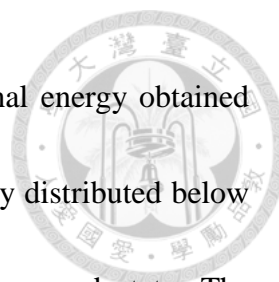


Figure 3-3. H atom TOF spectra at 213 nm. Black line represents the spectrum at crossing point. Red line represents the spectrum at 5.5 mm upstream of molecular beam. The intensity of different positions are scaled with different factor for comparison



Component III is not obvious in the TOF spectrum of 0 mm because of the large intensities of components I and II. Component III is buried in component II and it becomes clear when the intensity of component II decreases. Because the acceptance angle of the detector, the fragments forming in the first 2.5 μs were detected when pump laser was located at 0 mm, while the fragments forming in the 0.5-6.5 μs were detected at 5.5 mm. The relative intensity changes of these three components indicate that the components I and II after subtracting component III are produced within 0.5 μs and the generation of the component III can last to longer than 0.5 μs . We assigned components I and II to the dissociation in the electronic excited state and component III to the dissociation of highly vibrationally excited phenol in the electronic ground state.

The corresponding translational energy distributions are illustrated in Figure 3-4. The translational energy distribution obtained from the pump laser located at 0 mm shows two components. The fastest component, corresponding to the component I in TOF spectra, centers at $\sim 12000\text{ cm}^{-1}$ and reaches the maximum available energy. We assigned the fastest component as dissociation in the electronic excited state forming electronic ground state phenoxy radical product. The slow component with translational energy $< 8000\text{ cm}^{-1}$, corresponding to the component II in TOF spectra, peaks at 2000 cm^{-1} . Two dissociation channels contribute to this slow component: dissociation in the electronic excited state forming phenoxy radical in the electronic



excited A state, or dissociation in the ground state. The translational energy obtained from the pump laser beam located at 5.5 mm (component III) mainly distributed below 3000 cm^{-1} . It is solely contributed from the dissociation in the ground state. The translation energy distributions of dissociation in the excited state producing phenoxy radicals in A state can be obtained by subtracting the component III from component II with proper factor as described in chapter 2.

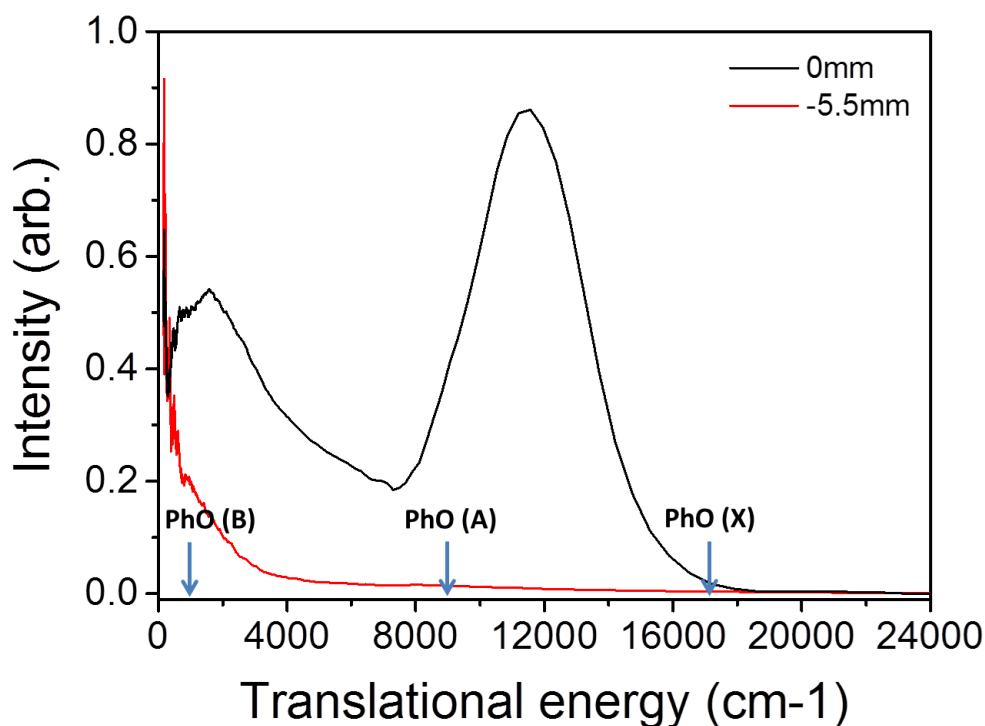
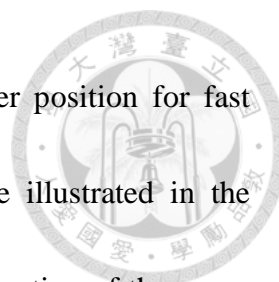


Figure 3-4. Translational energy distribution of H atom elimination channel at 213 nm. Vertical arrows indicate the maximum available energy of one photon dissociation to the phenoxy radical ground state, A state, and B state respectively. Black line represents the spectrum at crossing point. Red line represents the spectrum at 5.5 mm upstream of molecular beam. The intensity of different positions are scaled with different factor for comparison



The signal intensity change as the function of the pump laser position for fast component ($>10000\text{ cm}^{-1}$) and slow component ($<3000\text{ cm}^{-1}$) are illustrated in the Figure 3-3. As described in chapter 2, the intensity change as the function of the pump laser position for fast component can be regarded as an instrument response function $D(P)$ related to the distribution of pump laser beam, the detector acceptance region x_1 and x_2 . $D(p)$ become zero when $p < -5$ and thus the slow component at position $p < -5$ is mainly from component III. We fit the intensity of slow component as the function of pump laser position when $p < -5$ with the third term of Equation (2-15) to get the relative branching ratio and lifetime of ground state dissociation channel as illustrated in Figure 3-5. The fitted lifetime is $1.5 \pm 0.3\ \mu\text{s}$.

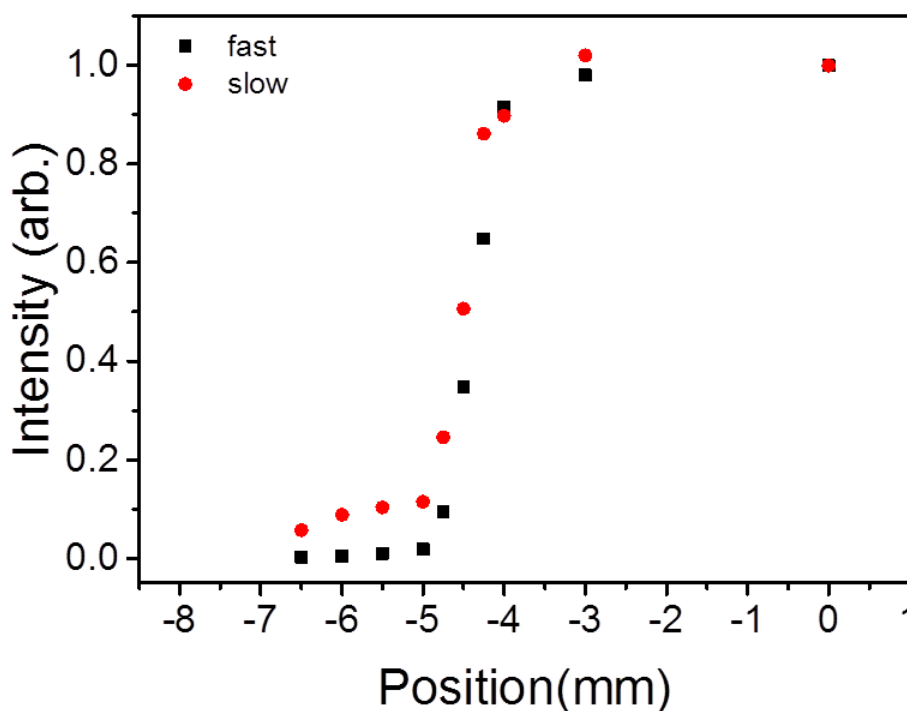


Figure 3-5. Intensity change as the function of the pump laser position at 213 nm for fast component (black square) and slow component (red dot) respectively

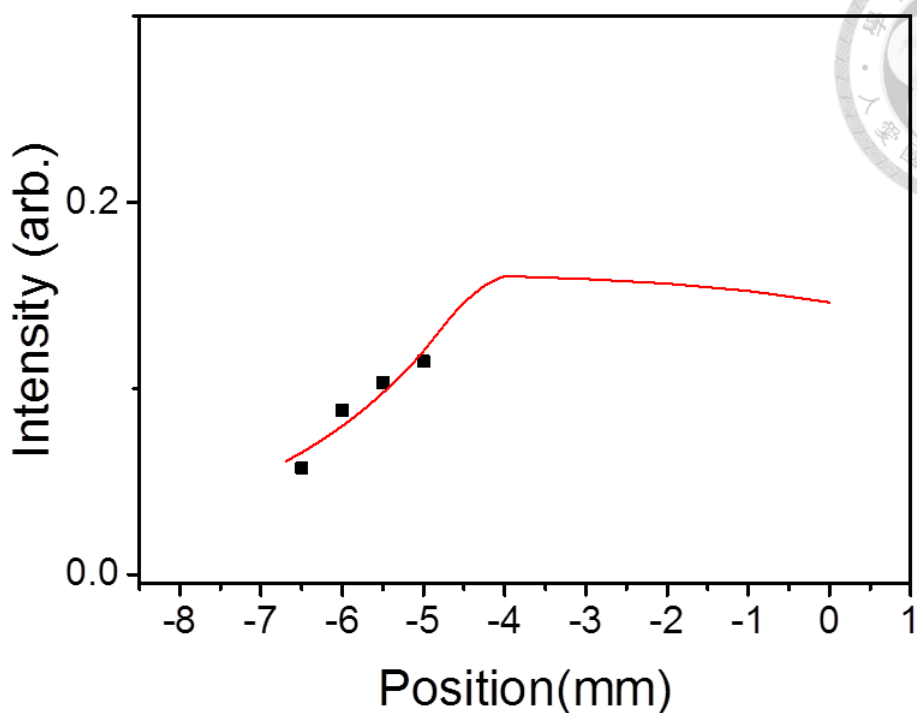


Figure 3-6. Fitting of Relative intensity change of slow component as the function of position at 213 nm. Solid square represents the experimental value. Red line represents the fitting curve. The fitting lifetime is $1.5 \pm 0.3 \mu\text{s}$.

From Figure 3-6, we can find the contribution of component III at the crossing point and subtract it from the spectrum to get the translational energy distribution of excited state dissociation and deconvolute it with two components, i.e. dissociation in the excited state forming phenoxy radical X and A state, as shown in Figure 3-7. Finally we can get the relatively branching ratio of OH bond fission of different dissociation channel as 0.07, 0.60, 0.32 for ground state dissociation and excited state dissociation forming phenoxy radical X and A state respectively.

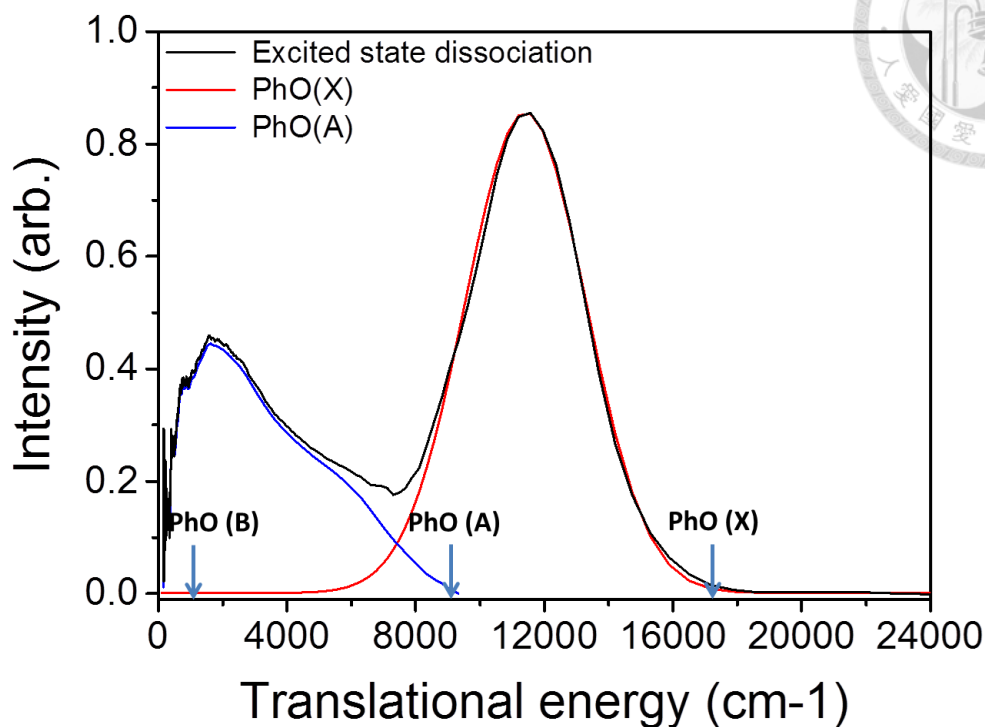


Figure 3-7. Translational energy distribution of excited state dissociation channel at 213 nm. Vertical arrows indicate the maximum available energy of one photon dissociation to the phenoxy radical ground state, A state, and B state respectively. Black line is the experimental data. Blue line and red line are the deconvolution results of black line.

Anisotropic parameter β_2 is also calculated by measuring the signal change with the angle of laser polarization and fit with the equation as shown in Figure 3-8. The fitting β_2 for the fast component is 0.1 ± 0.05 , a small but non-zero value. This is an indication that lifetime of fast component is less than 100 ps, which is in consistence with the assignment of dissociation in the repulsive state.

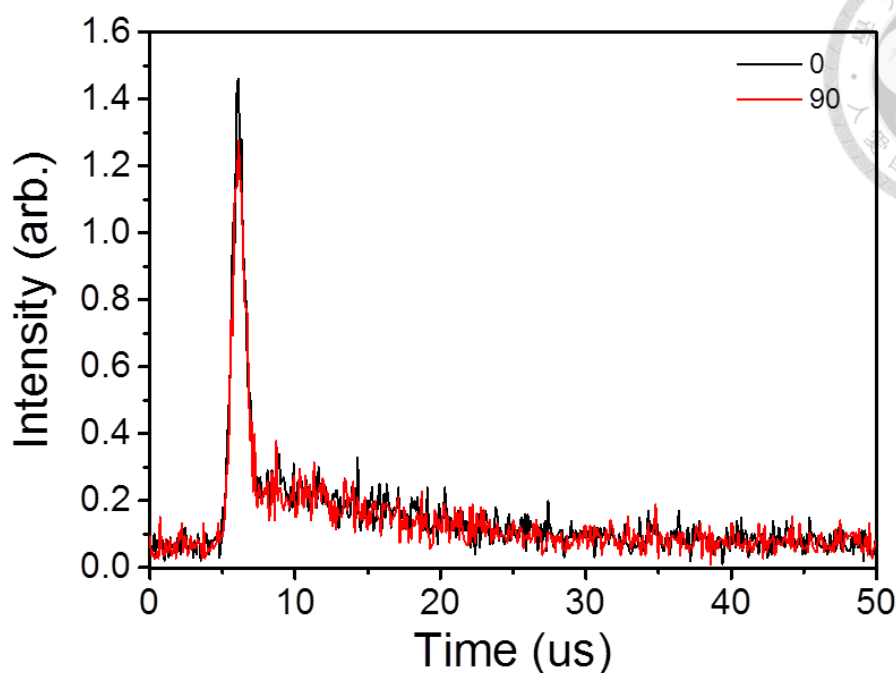


Figure 3-8. Signal change with the angle of laser polarization at 213 nm. Black line represents the laser polarization parallel to the detection axis. Red line represents the laser polarization perpendicular to the detection axis.

3.3 Photodissociation Experiment of Phenol at 193 nm

The H atom TOF spectra are illustrated in Figure 3-9 for two pump laser positions, at the crossing point (0 mm) and at the second position (7 mm upstream of molecular beam). Two components in the TOF spectrum of 0 mm can be observed: a sharp and fast component (component I) at arrival time 5-10 μs and a broad and slow component (component II) located from 10 μs to 30 μs . When the pump laser was moved 5.5 mm upstream of the molecular beam, the shape of the TOF spectra changed. The components I and II in the TOF spectrum become small and the third component (component III) located in the region from 20 μs to 200 μs can be clearly observed.

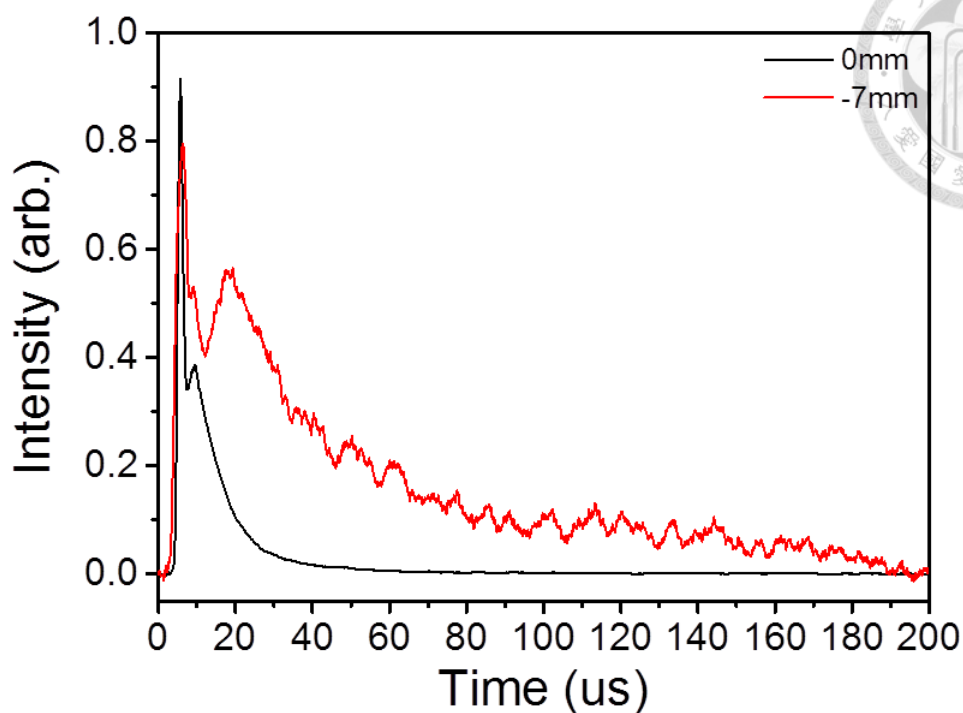


Figure 3-9. H atom TOF spectra at 193 nm. Black line represents the spectrum at crossing point. Red line represents the spectrum at 7 mm upstream of molecular beam. The intensity of different positions are scaled with different factor for comparison

Component III is not obvious in the TOF spectrum of 0 mm because of the large intensities of components I and II. Component III is buried in component II and it becomes clear when the intensity of component II decreases. Because the acceptance angle of the detector, the fragments forming in the first 2.5 μs were detected when pump laser was located at 0 mm, while the fragments forming in the 1-7 μs were detected at 7 mm. The relative intensity changes of these three components indicate that the components I and II after subtracting component III are produced within 1 μs and the generation of the component III can last to longer than 1 us. We assigned components I

and II to the dissociation in the electronic excited state and component III to the dissociation of highly vibrationally excited phenol in the electronic ground state.

The corresponding translational energy distributions are illustrated in Figure 3-10.

The translational energy distribution obtained from the pump laser located at 0 mm shows two components. The fastest component, corresponding to the component I in TOF spectra, centers at ~ 13000 cm^{-1} and reaches the maximum available energy. We assigned the fastest component as dissociation in the electronic excited state forming electronic ground state phenoxy radical product. The slow component with translational energy < 8000 cm^{-1} , corresponding to the component II in TOF spectra, peaks at 3000 cm^{-1} . Three dissociation channels contribute to this slow component: dissociation in the electronic excited state forming phenoxy radical in the electronic excited A state or B state, or dissociation in the ground state. The translational energy obtained from the pump laser beam located at 7 mm (component III) mainly distributed below 2000 cm^{-1} . It is solely contributed from the dissociation in the ground state. The translation energy distributions of dissociation in the excited state can be obtained by subtracting the component III from component II with proper factor as described in chapter 2.

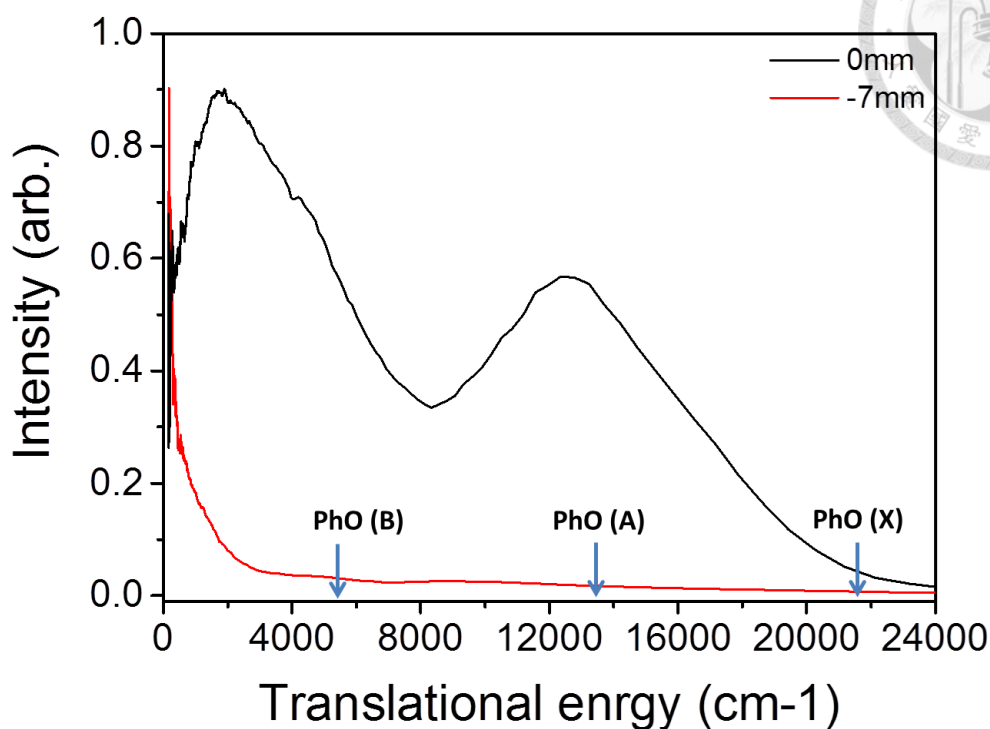
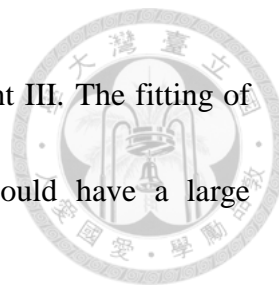


Figure 3-10. Translational energy distribution of H atom elimination channel at 193 nm. Vertical arrows indicate the maximum available energy of one photon dissociation to the phenoxy radical ground state, A state, and B state respectively. Black line represent the spectrum at crossing point. Red line represent the spectrum at 7 mm upstream of molecular beam. The intensity of different positions are scaled with different factor for comparison

The signal intensity change as the function of the pump laser position for fast component ($>12000 \text{ cm}^{-1}$) and slow component ($<1000 \text{ cm}^{-1}$) is illustrated in the Figure 3-11. As described in chapter 2, the intensity change as the function of the pump laser position for fast component can be regarded as an instrument response function $D(P)$ related to the distribution of pump laser beam, the detector acceptance region x_1 and x_2 . Because the beam size of excimer laser beam is large, $D(p)$ become zero until $p < -7$ and



thus the slow component at position $p < -7$ is mainly from component III. The fitting of the slow component with the third term of Equation (2-15) would have a large uncertainty due to the large beam size.

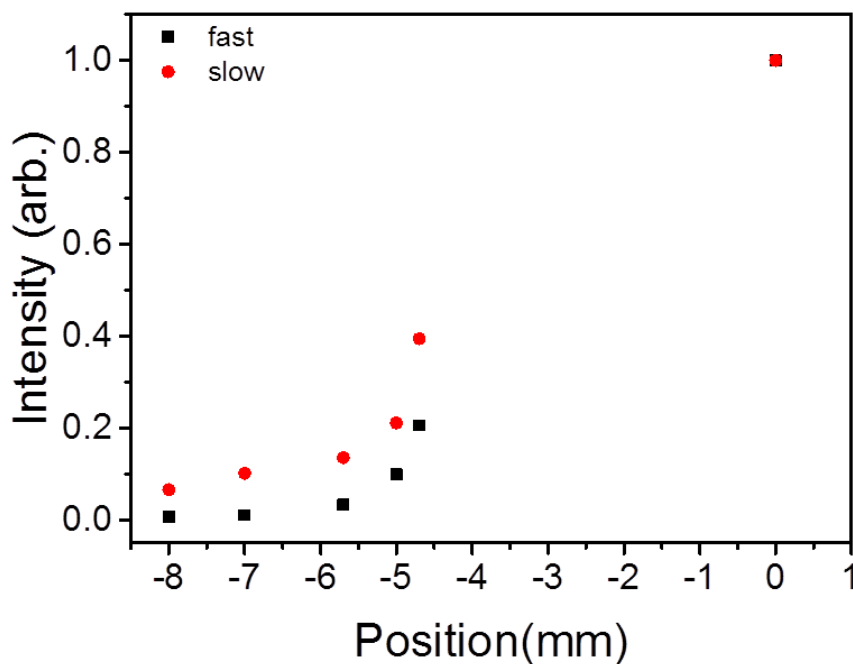


Figure 3-11. Intensity change as the function of the pump laser position at 193 nm for fast component (black dot) and slow component (red dot) respectively

Here, we use another time-resolved pump-probe apparatus to measure the transient ion yield and determine the lifetime of highly vibrational electronic ground state phenol first. The TOF-MS spectrum is shown in the figure 3-12. Five different ions with $m/z = 65, 66$ (small amount), 93, 94, and 95 can be observed. Ions with $m/z = 94$ and 95 are phenol parent molecular and its isotope. Others ion are fragment. According to previous work, the corresponding ions are $C_5H_5^+$, $C_5H_6^+$, and $C_6H_5O^+$. The dissociation and ionization scheme are listed as bellowed :

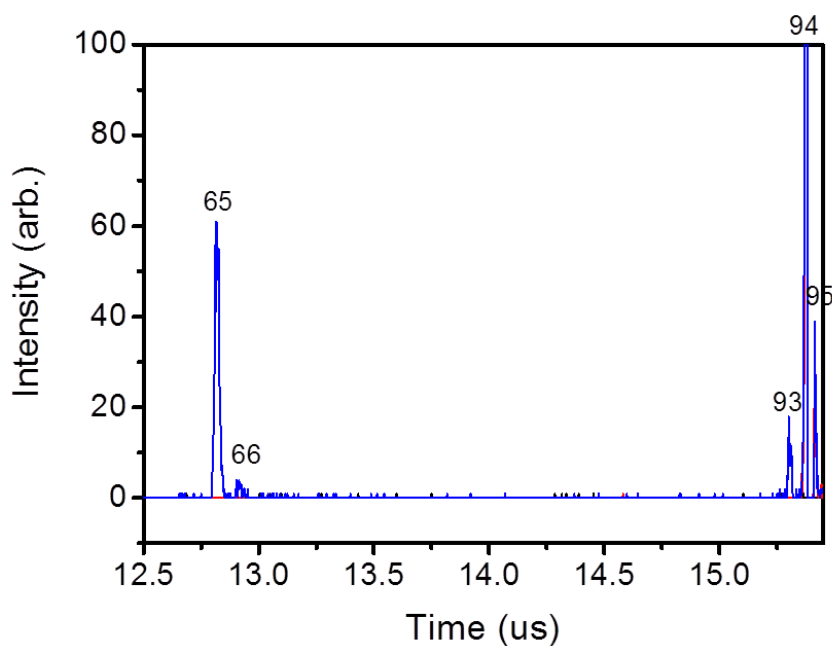
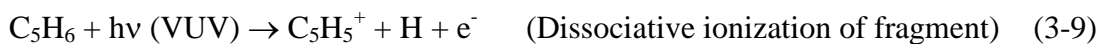
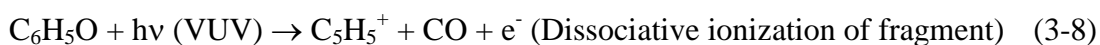
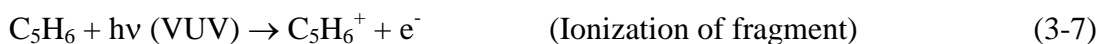
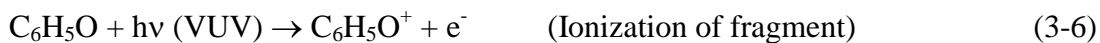
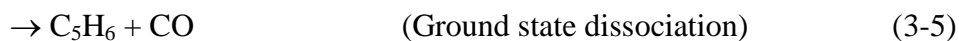
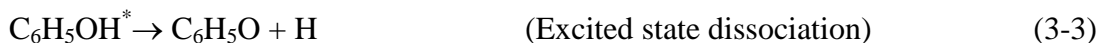


Figure 3-12. Time-of-Fight mass spectrum with 193 nm pump and 118 nm probe



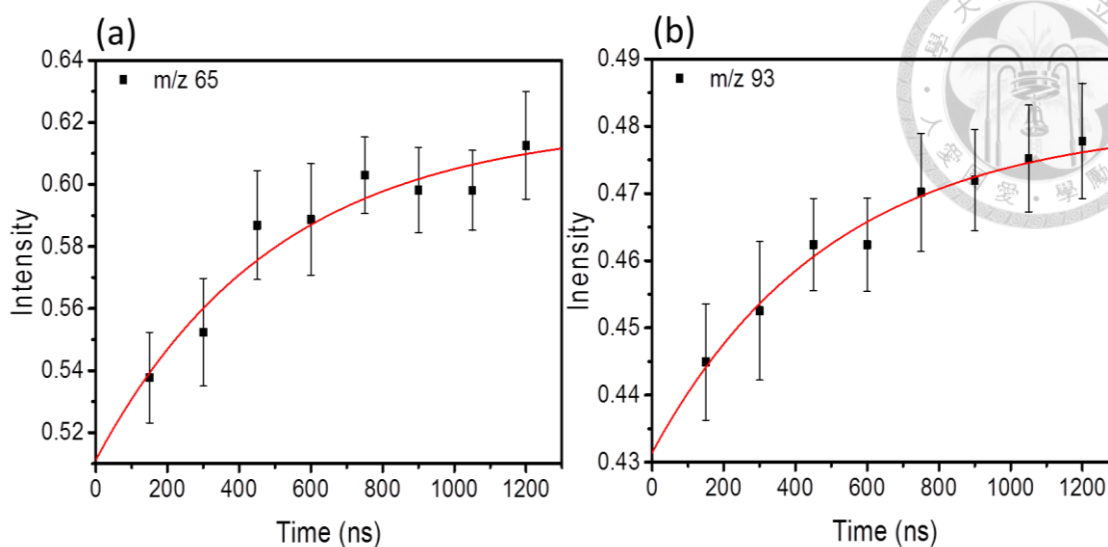
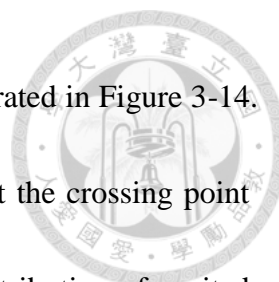


Figure 3-13. Transient ion yield of (a) $C_5H_5^+$, (b) $C_6H_5O^+$ at 193 nm. Solid square represent the experimental value of 512*8 laser shots. Error bar is twice of the standard deviation of the mean. Red line is the fitting curve with equation $A + B \times e^{-t/\tau}$.

The $C_6H_5O^+$ ions come from ionization reaction (3-6), of which neutral molecules are from reactions (3-3) and (3-4). Thus, the transient ion yield of fragments with m/z = 93 can be fitted with the equation $A + B \times e^{-t/\tau}$, where τ is the lifetime of highly vibrational electronic ground state. The $C_5H_5^+$ ions are from dissociative ionization reaction (3-8) and (3-9), of which neutral molecules come from reaction (3-3), (3-4) and (3-5). Therefore, the transient ion yield of fragments with m/z = 65 can be fitted with the equation $C + D \times e^{-t/\tau}$. The transient ion yield of $C_6H_5O^+$ and $C_5H_5^+$ are shown in Figure 3-13, and the fitting lifetime is 500 ± 200 ns.

We use the obtained lifetime to fit the intensity of slow component as the function of pump laser position when $p < -5.5$ with the third term of Equation (2-15) to get the



relative branching ratio of ground state dissociation channel as illustrated in Figure 3-14.

From Figure 3-14, we can find the contribution of component III at the crossing point and subtract it from the spectrum to get the translational energy distribution of excited state dissociation and deconvolute it with three components, i.e. dissociation in the excited state forming phenoxy radical X, A, and B state, as shown in Figure 3-15.

Finally we can get the relatively branching ratio of OH bond fission of different dissociation channel as 0.05, 0.53, 0.24, 0.17 for ground state dissociation and excited state dissociation forming phenoxy radical X,A, and B state respectively.

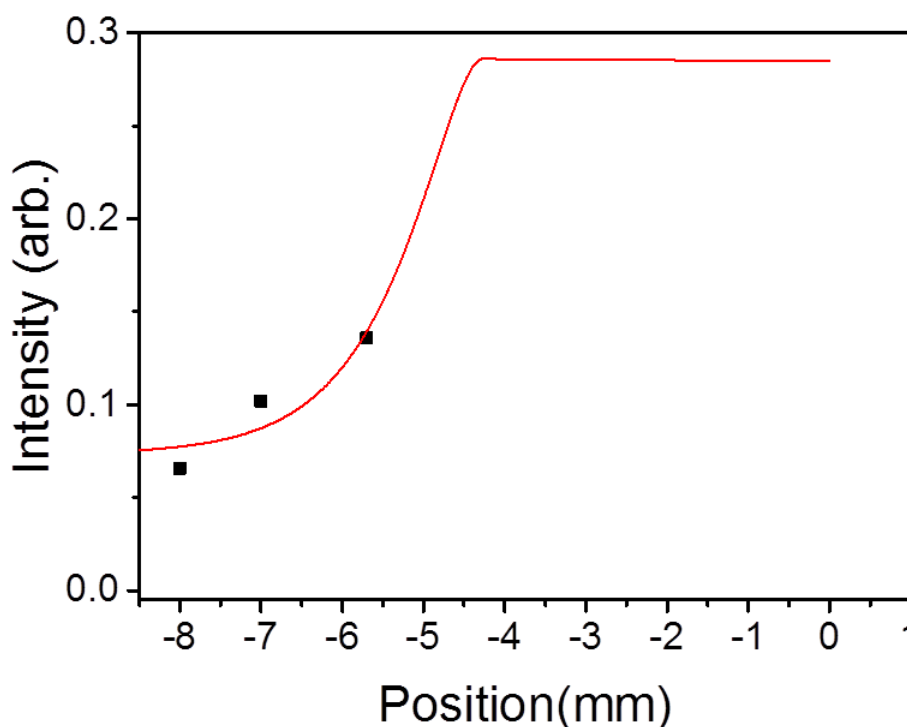


Figure 3-14. Fitting of relative intensity change of slow component as the function of position at 193 nm. Solid square represent the experimental value. Red line represents the fitting curve.

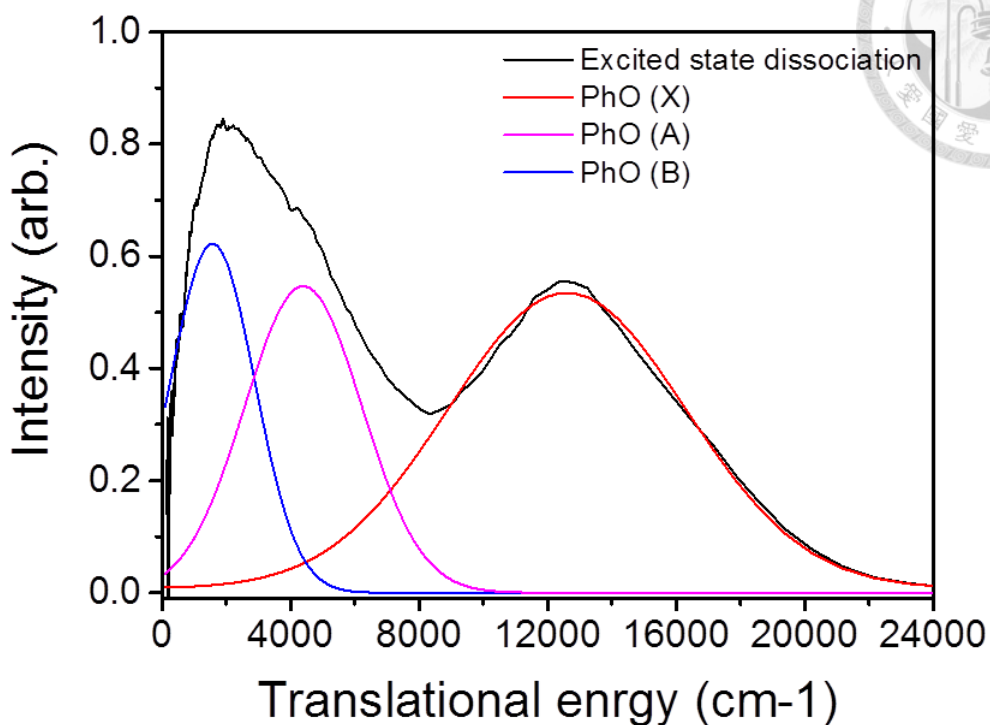


Figure 3-15. Translational energy distribution of excited state dissociation channel at 193 nm. Vertical arrows indicate the maximum available energy of one photon dissociation to the phenoxy radical ground state, A state, and B state respectively. Black line is the experimental data. Blue, pink, and red lines are the deconvolution results of black line

Anisotropic parameter β_2 is also calculated by measuring the signal change with the angle of laser polarization and fit with the equation as shown in Figure 3-16. The fitting β_2 for the fast component is 0.2 ± 0.1 , a small but non-zero value. This is an indication that lifetime of fast component is less than 100 ps, which is in consistence with the assignment dissociation in the repulsive state.

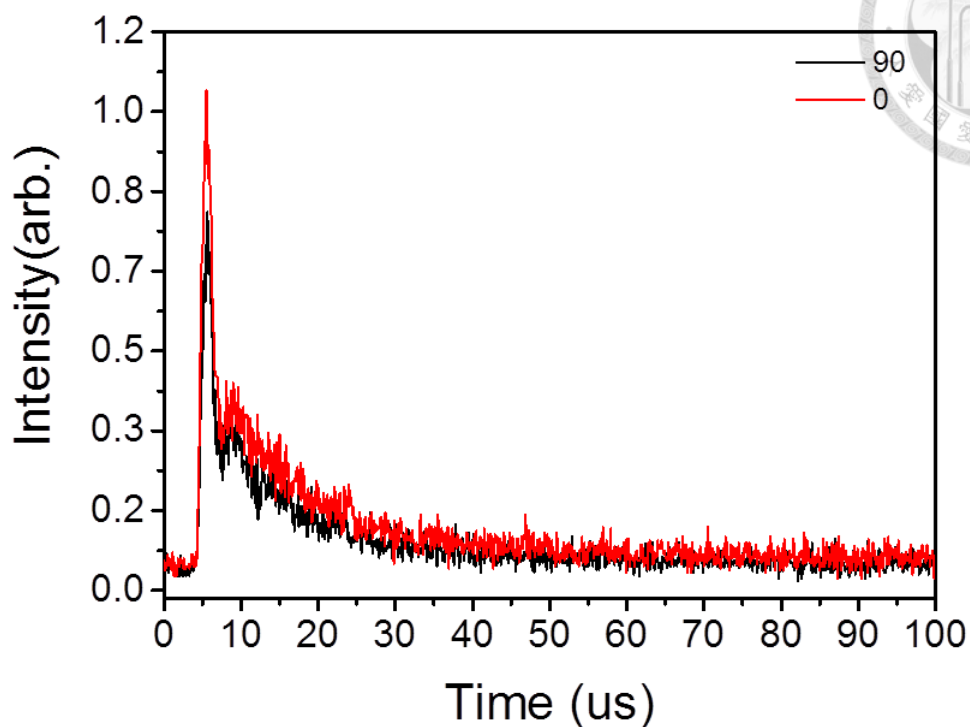


Figure 3-16. Signal change with the angle of laser polarization at 193 nm. Black line represents the laser polarization parallel to the detection axis. Red line represents the laser polarization perpendicular to the detection axis.

3.4 Discussions

We compare the translational energy distribution at 213 nm and 193 nm for both ground state dissociation and excited state dissociation channel. Figure 3-17 shows the comparison of ground state dissociation. The distribution of 213 nm mainly distributed below 3000 cm^{-1} , while that of 193 nm mainly distributed below 2000 cm^{-1} . It seems that there is an additional component at translational energy $2000\sim 3000\text{ cm}^{-1}$. It is strange that with decreasing photon energy, the translational energy increase.

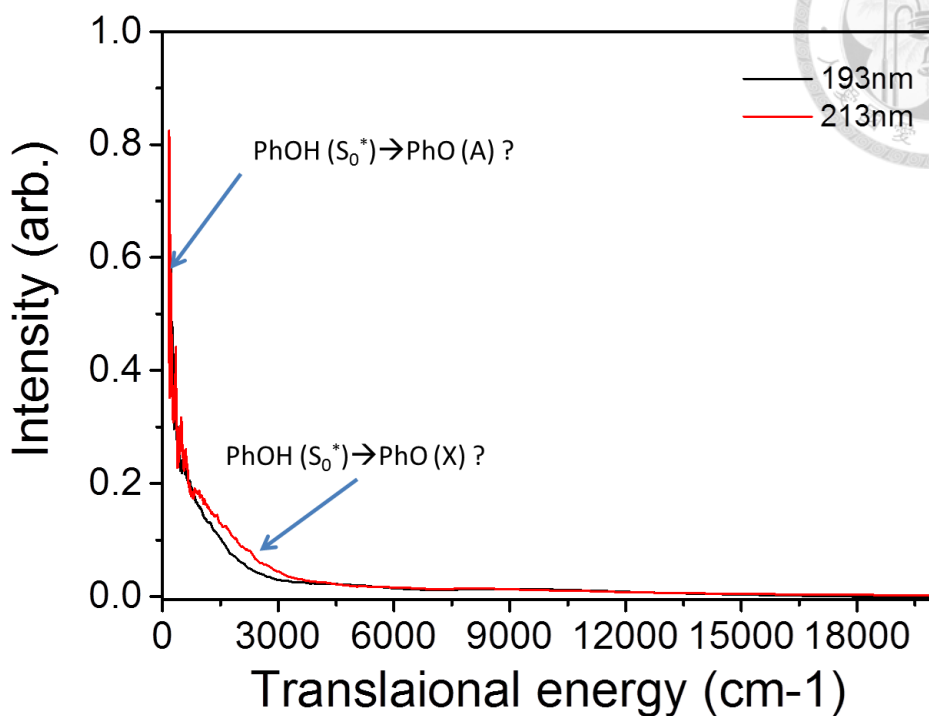
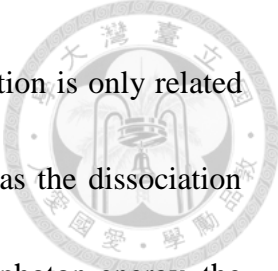


Figure 3-17. Comparison of ground state dissociation at 193 nm (black line) and 213 nm (red line)

One possible explanation is that we can assign the component with higher energy as the formation of phenoxy radical X state and the component with lower energy as the formation of phenoxy radical A state. In such case, the difference of the spectrum is due to the branching ratio change of these two products and we can apply Landau–Zener theory to explain it. Landau–Zener theory describes the probability of diabatic transition when molecule passes through the conical intersection:³¹

$$P_{\text{diabatic}} = \exp\left(-2\pi \frac{V_{12}}{(\partial E / \partial t)}\right) = \exp\left(-2\pi \frac{V_{12}}{(\partial E / \partial q) * (\partial q / \partial t)}\right) \quad (3-10)$$

where V_{12} is the coupling of two potential, E is the energy difference of two potential t is time, and q is the displacement of the potential energy surface. For a given molecule,



V_{12} and $(\partial E/\partial q)$ are constant and the probability of diabatic transition is only related to the $(\partial q/\partial t)$. For the photodissociation case, q is the same axis as the dissociation axis and $(\partial q/\partial t)$ is related to the recoil velocity. With increasing photon energy, the initial recoil velocity would increase and thus the probability of daibatic transition would increase. For ground dissociation channel, the diabatic transition would populate to the phenoxy radical A state. Thus, with increasing photon energy the translational energy distribution would populate to a lower energy part. This may be a possible explanation. Yet, after internal conversion, the energy would randomize at each degree of freedom and it is hard to have enough energy to populate to the A state of phenoxy radical. The existence channel of ground state dissociation forming phenoxy radical A state is still under debate.

The comparison of excited state dissociation channel is show in Figure 3-18. The distributions of these two wavelengths are both bimodal. The translation energy at 193 nm is larger than that at 213 nm and it is reasonable due to the increasing photon energy. The slow component at 193 nm is more than that at 213 nm. This may be due to the existence of phenoxy radical B state at 193nm photolysis.

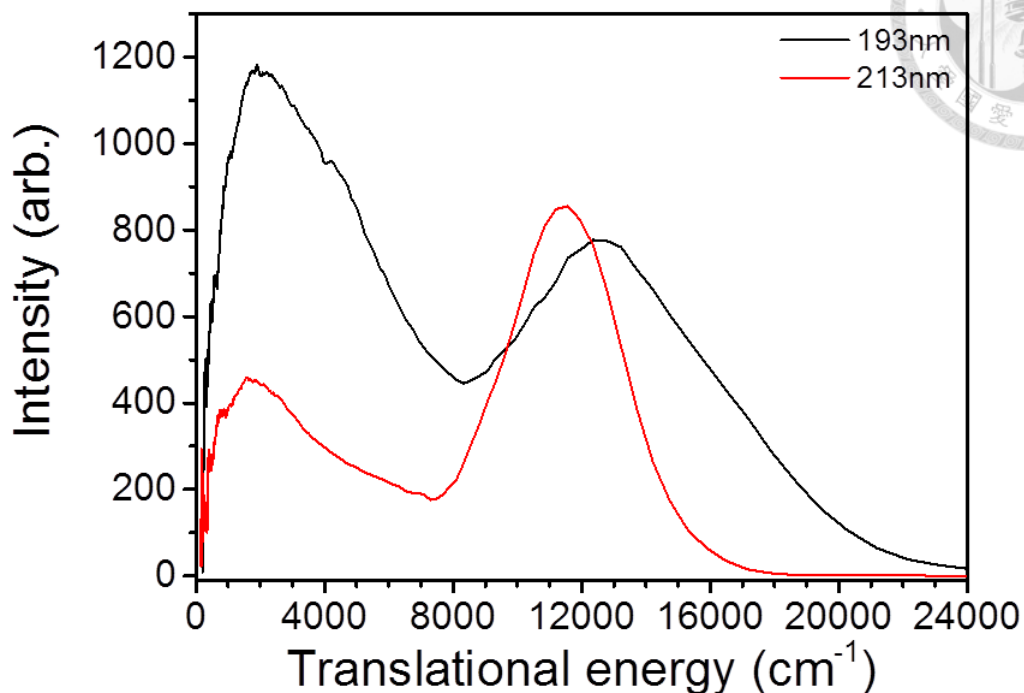
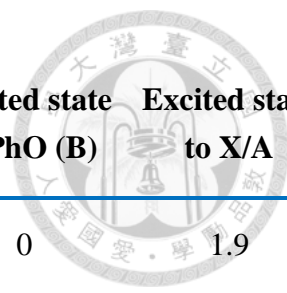


Figure 3-18. Comparison of excited state dissociation at 193 nm (black line) and 213 nm (red line)

Finally, we compare the branching ratio at these two wavelengths for different dissociation channel. The result is shown in Table 3-1. For the branching ratio of ground state dissociation channel, 213 nm is larger than the 193 nm. Notice that the branching ratio here is just related to the contribution of OH bond fission and not equal to the quantum yield of internal conversion process because there are other fragment, CO and H₂O elimination, after internal conversion. For the excited state dissociation, we calculate the ratio of phenoxy radical X state to A state. The branching of phenoxy radical excited state is larger at 213 nm than that of 193nm and this is in consistence with Landau–Zener theory.



Wavelength	Ground state dissociation	Excited state to PhO (X)	Excited state to PhO (A)	Excited state to PhO (B)	Excited state to X/A
213nm	0.07±0.02	0.60±0.06	0.32±0.04	0	1.9
193nm	0.05±0.02	0.53±0.05	0.24±0.03	0.17±0.03	2.2

Table 3-1. Comparison of the branching ratio at 193 nm and 213 nm for different dissociation channel

Chapter 4. Prospects



We have demonstrated a new experimental method and succeeded in the investigation of photodissociation of phenol. The advantage of our new method is that we can measure time-resolved photofragment translational energy distribution without producing any artificial background. This is useful for investigating other large molecules which would also dissociate on the multi potential energy surface, such as aniline or anisole.

Photodissociation of aniline has been studied by other experiments previously.³²⁻³⁴ The main dissociation channel is NH bond fission. The 1D potential energy surface cut along NH axis is shown in Figure 4-1.³³ It is similar to the potential energy surface cut of phenol, but the electronic energy gap of product radical (~ 2.3 eV) is much larger than that of phenol (~ 1 eV). The photofragment translational energy distributions at 193 nm photolysis are illustrated in Figure 4-2 with two different methods.³²⁻³³ The results also show bimodal shape of the distribution like phenol. The fast component was assigned as dissociation in the repulsive state and the slow component was assigned as dissociation in the ground state after internal conversion. There was no assignment of dissociation in the repulsive state forming excited state anilino radical before. Yet, from the energetic view, it is possible to generate anilino radical in its electronic excited state. We can use our new method to check whether the excited anilino radical exist or not.

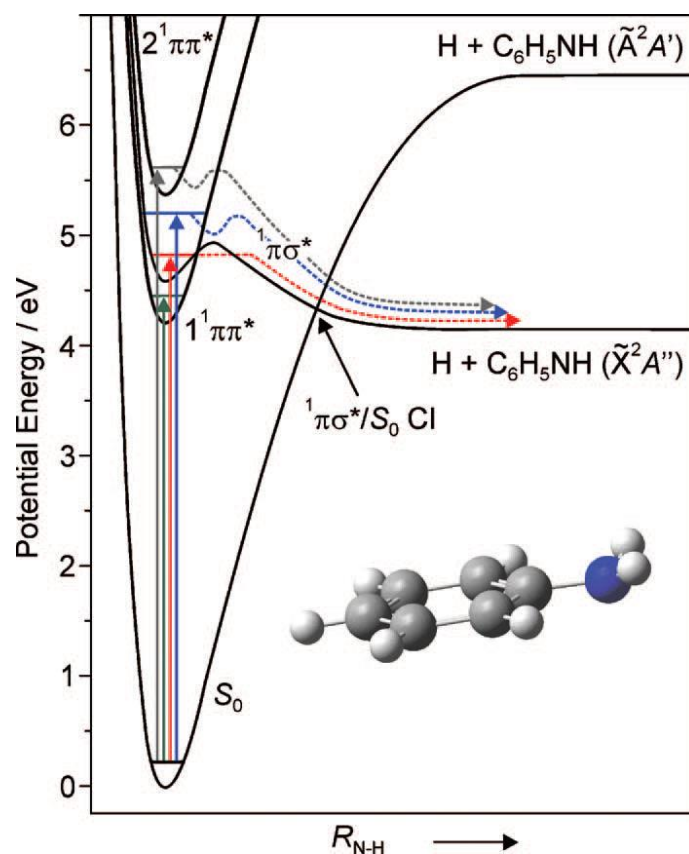
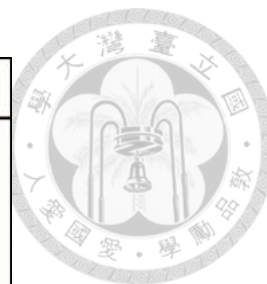


Figure 4-1. 1D Potential energy surface cut of aniline along NH axis.³³

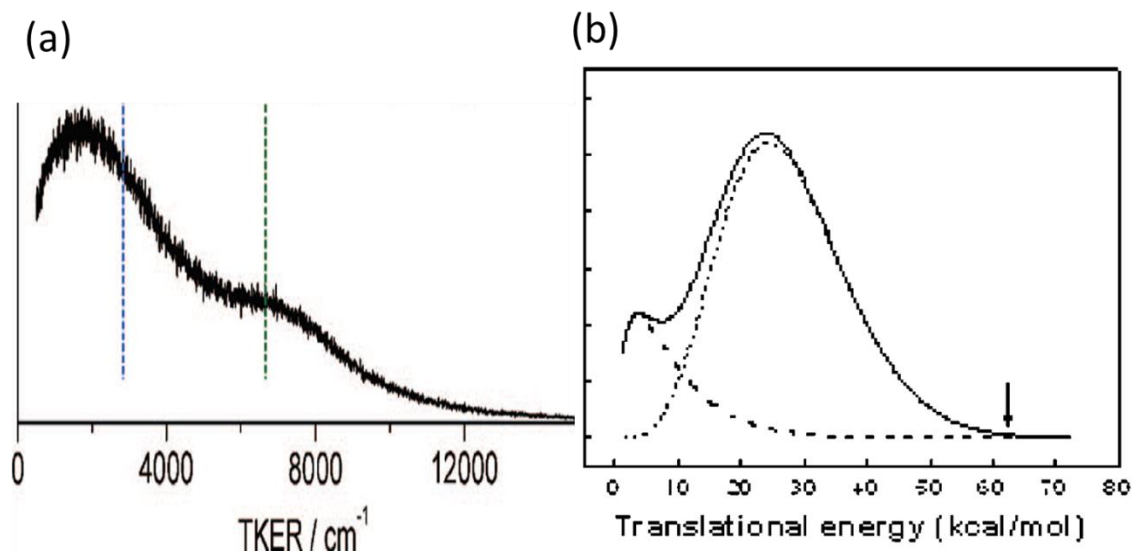


Figure 4-2. Photofragment translational energy distributions of aniline at 193 nm using (a) H Rydberg atom tagging³³ and (b) multi mass ion imaging³².

Photodissociation of anisole has been studied by our group previously.³⁵ The main dissociation channel is CH₃ elimination channel producing phenoxy radical plus methyl radical. The photofragment translational energy distributions at 193 nm photolysis are illustrated in Figure 4-3. It is also a bimodal shape of distribution and the relative amount of slow component is much larger than that of phenol. We previously assigned the slow component as dissociation in the ground state and thus the internal conversion quantum yield of anisole should be much larger than phenol. Recently, the results of photodissociation of mequinol suggested that it is easier to produce phenoxy radical in its electronic excited state in the case of O-CH₃ bond fission than that of OH bond fission.³⁶ It may be the reason that the slow component of anisole is much larger than the phenol. We can use our new method to check what the origin of the change of relative amount of slow component is.

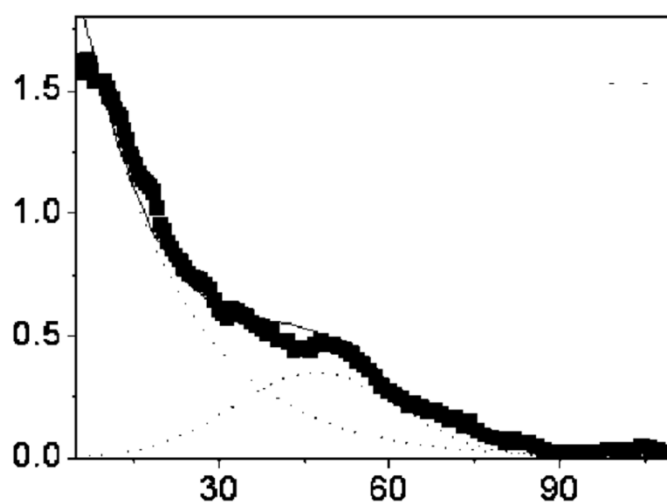


Figure 4-3. Photofragment translational energy distributions of anisole at 193 nm using multi mass ion imaging.

Chapter 5. Conclusions

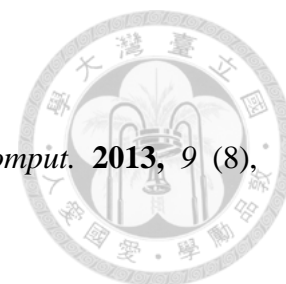


In this work, we have modified conventional photofragment translational spectroscopy to perform a new type of time-resolved experiment and get the time-resolved spectra of photofragment translational energy distribution of phenol. The results show clear characteristics of three different dissociation channels. Two of them having a lifetime less than 10 ns with the contributions to translational energy center at about 12000 cm^{-1} and 2000 cm^{-1} are assigned as dissociation in the phenol excited state forming phenoxy radical in the ground state and excited state respectively. The third channel with a lifetime larger than 100 ns contributes a component mainly below 3000 cm^{-1} in the translational energy distribution. This is the first time that the contribution of dissociation in ground state and in excited state can be differentiated by their lifetime. Finally, we get the branching ratio of ground state dissociation channel and excited state dissociation channel forming phenoxy radical X,A,B state for the photodissociation of phenol at 193nm as 0.05, 0.53, 0.24, 0.17, and at 213 nm as 0.07, 0.60, 0.32, 0. These branching ratios are useful for justifying the results of theoretical calculations. Furthermore, this technique is useful for the investigation of photodissociation of other molecules which would also dissociate on the multi potential energy surface such as aniline or anisole.



Reference

1. Pino, G. A.; Dedonder-Lardeux, C.; Grégoire, G.; Jouvét, C.; Martrenchard, S.; Solgadi, D., *J. Chem. Phys.* **1999**, *111* (24), 10747-10749.
2. Pino, G.; Grégoire, G.; Dedonder-Lardeux, C.; Jouvét, C.; Martrenchard, S.; Solgadi, D., *Phys. Chem. Chem. Phys.* **2000**, *2* (4), 893-900.
3. Tseng, C. M.; Lee, Y. T.; Ni, C. K., *J. Chem. Phys.* **2004**, *121* (6), 2459-61.
4. Nix, M. G.; Devine, A. L.; Cronin, B.; Dixon, R. N.; Ashfold, M. N., *J. Chem. Phys.* **2006**, *125* (13), 133318.
5. Tseng, C.-M.; Lee, Y. T.; Lin, M.-F.; Ni, C.-K.; Suet-Yi Liu; Lee, Y.-P.; Xu, Z. F.; Lin, M. C., *J. Phys. Chem. A* **2007**, *111*, 9463-9470.
6. Iqbal, A.; Pegg, L.-J.; Stavros, V. G., *J. Phys. Chem. A* **2008**, *112*, 9531–9534.
7. Iqbal, A.; Cheung, M. S. Y.; Nix, M. G. D.; Stavros, V. G., *J. Phys. Chem. A* **2009**, *113*, 8157–8163.
8. King, G. A.; Oliver, T. A. A.; Nix, M. G. D.; Ashfold, M. N. R., *J. Phys. Chem. A* **2009**, *113*, 7984–7993.
9. Pino, G. A.; Oldani, A. N.; Marceca, E.; Fujii, M.; Ishiuchi, S. I.; Miyazaki, M.; Broquier, M.; Dedonder, C.; Jouvét, C., *J. Chem. Phys.* **2010**, *133* (12), 124313.
10. Roberts, G. M.; Chatterley, A. S.; Young, J. D.; Stavros, V. G., *J. Phys. Chem. Lett.* **2012**, *3* (3), 348-52.
11. Lee, C.; Lin, Y.-C.; Lee, S.-H.; Lee, Y.-Y.; Tseng, C.-M.; Lee, Y.-T.; Ni, C.-K., *THE JOURNAL OF CHEMICAL PHYSICS* **2017**, *147*.
12. Sobolewski, A. L.; Domcke, W., *J. Phys. Chem. A* **2001**, *105*.
13. Sobolewski, A. L.; Domcke, W.; Dedonder-Lardeux, C.; Jouvét, C., *Phys. Chem. Chem. Phys.* **2002**, *4* (7), 1093-1100.
14. Dixon, R. N.; Oliver, T. A.; Ashfold, M. N., *J. Chem. Phys.* **2011**, *134* (19),



194303.

15. Xu, X.; Yang, K. R.; Truhlar, D. G., *J. Chem. Theory. Comput.* **2013**, *9* (8), 3612-25.

16. Xu, X.; Zheng, J.; Yang, K. R.; Truhlar, D. G., *J. Am. Chem. Soc.* **2014**, *136* (46), 16378-86.

17. Yang, K. R.; Xu, X.; Zheng, J.; Truhlar, D. G., *Chem. Sci.* **2014**, *5* (12), 4661-4680.

18. Guo, H.; Yarkony, D. R., *Phys. Chem. Chem. Phys.* **2016**, *18* (38), 26335-26352.

19. Xie, C.; Ma, J.; Zhu, X.; Yarkony, D. R.; Xie, D.; Guo, H., *J. Am. Chem. Soc.* **2016**, *138* (25), 7828-31.

20. Xie, C.; Yarkony, D. R.; Guo, H., *Phy. Rev. A* **2017**, *95* (2).

21. Callis, P. R., *Annu. Rev. Phys. Chem.* **1983**, *34*, 329-357.

22. creed, D., *Photochem. Photobiol.* **1984**, *39*, 537-562.

23. Creed, D., *Photochem. Photobiol.* **1984**, *39*, 537.

24. Lee, C.; Lin, Y.-C.; Lee, S.-H.; Lee, Y.-Y.; Tseng, C.-M.; Lee, Y.-T.; Ni, C.-K., *J. Chem. Phys.* **2017**, *147* (1), 013904.

25. Ratzner, C.; Kupper, J.; Daniel Spangenberg²; Schmitt, M., *Chem. Phys.* **2002**, *283*, 153-169.

26. Wang, C. C.; Lee, Y. T.; Lin, J. J.; Shu, J.; Lee, Y.-Y.; Yang, X., *J. Chem. Phys.* **2002**, *117* (1), 153-160.


27. Lin, J. J.; Chen, Y.; Lee, Y. Y.; Lee, Y. T.; Yang, X., *Chem. Phys. Lett.* **2002**, *361*, 374-382.

28. Lee, S. H.; Chen, W. K.; Huang, W. J., *J. Chem. Phys.* **2009**, *130* (5), 054301.

29. Scoles, G., *Atomic and molecular beam methods*. 1988.

30. Yang, S. c.; Bersohn, R., *J. Chem. Phys.* **1974**, *61* (11), 4400-4407.

31. Wittig, C., *J. Phys. Chem. B* **2005**, *109*, 8428-8430.

- 
32. Tseng, C.-M.; Dyakov, Y. A.; Huang, C.-L.; Mebel, A. M.; Lin, S. H.; Lee, Y. T.; Ni, C.-K., *J. Am. Chem. Soc.* **2004**, *126*, 8760-8768.
33. King, G. A.; Oliver, T. A.; Ashfold, M. N., *J. Chem. Phys.* **2010**, *132* (21), 214307.
34. Roberts, G. M.; Williams, C. A.; Young, J. D.; Ullrich, S.; Paterson, M. J.; Stavros, V. G., *J. Am. Chem. Soc.* **2012**, *134* (30), 12578-89.
35. Tseng, C. M.; Lee, Y. T.; Ni, C. K., *J. Phys. Chem. A* **2009**, *113* (16), 3881-5.
36. Hadden, D. J.; Roberts, G. M.; Karsili, T. N.; Ashfold, M. N.; Stavros, V. G., *Phys. Chem. Chem. Phys.* **2012**, *14* (38), 13415-28.

Appendix A. Changing from laboratory frame to center-of-mass frame

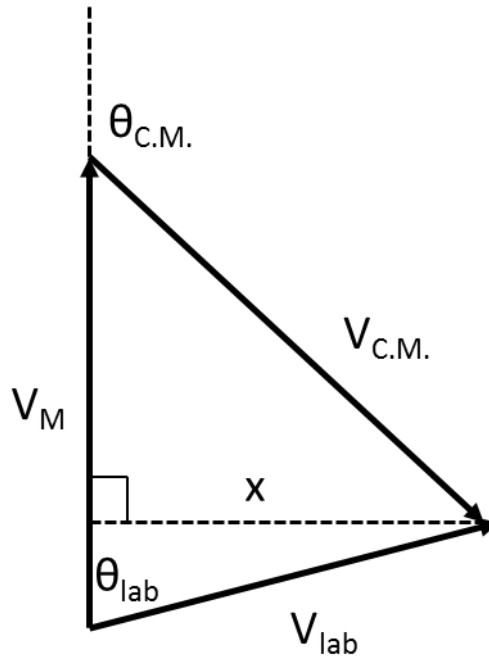


Figure A-1. Vector and angle correlation between laboratory frame and center-of-mass frame

Figure A-1 shows the relationship between laboratory frame and center-of-mass frame with V_M , $V_{C.M.}$, and V_{lab} represent the velocity of molecular beam, fragment velocity in the center-of-mass frame, and in the laboratory frame, and $\theta_{C.M.}$ and θ_{lab} represent the angle in the center-of-mass frame, and in the laboratory frame. According to Figure A-1, we can calculate x to connect $\theta_{C.M.}$ and θ_{lab} .

$$V_{C.M.} \sin(180 - \theta_{C.M.}) = x = (V_M - V_{C.M.} \cos(180 - \theta_{C.M.})) \tan \theta_{lab} \quad (A-1)$$

$$\Rightarrow V_{C.M.} \sin \theta_{C.M.} = (V_M + V_{C.M.} \cos \theta_{C.M.}) \tan \theta_{lab} \quad (A-2)$$

$$\Rightarrow \tan \theta_{lab} = \frac{V_{C.M.} \sin \theta_{C.M.}}{(V_M + V_{C.M.} \cos \theta_{C.M.})} = \frac{\sin \theta_{C.M.}}{\left(\frac{V_M}{V_{C.M.}} + \cos \theta_{C.M.}\right)} \quad (A-3)$$



Set $\frac{V_M}{V_{C.M.}} = r$, and from equation (A-3) we can get $\cos \theta_{lab}$:

$$\cos \theta_{lab} = \frac{1}{\sqrt{1 + \tan^2 \theta_{lab}}} = \frac{r + \cos \theta_{C.M.}}{\sqrt{r^2 + 2r \cos \theta_{C.M.} + 1}} \quad (A-4)$$

The relation between the differential cross section in the laboratory frame and center-of mass frame is:

$$\frac{d\sigma}{d\Omega_{Lab}} = \frac{d\sigma}{d\Omega_{C.M.}} * \frac{d\Omega_{C.M.}}{d\Omega_{Lab}} = \frac{d\sigma}{d\Omega_{C.M.}} * \frac{\sin \theta_{C.M.} d\theta_{C.M.} d\psi_{C.M.}}{\sin \theta_{lab} d\theta_{lab} d\psi_{lab}} = \frac{d\sigma}{d\Omega_{C.M.}} * \frac{d \cos \theta_{C.M.}}{d \cos \theta_{lab}} \quad (A-5)$$

where σ is the cross section and Ω_{lab} , $\Omega_{C.M.}$ represent the solid angle in the laboratory

frame and center-of mass frame. We can calculate $\frac{d \cos \theta_{C.M.}}{d \cos \theta_{lab}}$ using equation (A-4):

$$\frac{d \cos \theta_{C.M.}}{d \cos \theta_{lab}} = \frac{1}{\left(\frac{d \cos \theta_{lab}}{d \cos \theta_{C.M.}}\right)} = \frac{(1 + r^2 + 2r \cos \theta_{C.M.})}{1 + r \cos \theta_{C.M.}} \quad (A-6)$$

From equation (A-5) and (A-6), we can get equation (A-7):

$$\frac{d\sigma}{d\Omega_{Lab}} = \frac{d\sigma}{d\Omega_{C.M.}} * \frac{(1 + r^2 + 2r \cos \theta_{C.M.})}{1 + r \cos \theta_{C.M.}} \quad (A-7)$$

For the detection angle of $\theta_{lab} = 90^\circ$, $r = \frac{V_M}{V_{C.M.}} = \cos(180 - \theta_{C.M.}) = -\cos \theta_{C.M.}$, and

equation (A-7) can be rewritten as

$$\frac{d\sigma}{d\Omega_{Lab}} = \frac{d\sigma}{d\Omega_{C.M.}} * \frac{(1 + r^2 + 2r \cos \theta_{C.M.})}{1 + r \cos \theta_{C.M.}} = \frac{d\sigma}{d\Omega_{C.M.}} \frac{(1 - r^2)^{\frac{3}{2}}}{1 - r^2} = \frac{d\sigma}{d\Omega_{C.M.}} \sqrt{1 - \left(\frac{V_M}{V_{C.M.}}\right)^2} \quad (A-8)$$

Equation (A-8) is the same as Equation (2-6).